ABSTRACT

Title of dissertation: ORGANIC MOLECULAR THIN FILMS
                          ON DEVICE-RELEVANT SUBSTRATES

                          Michelle A. Groce,
                          Doctor of Philosophy, 2013

Dissertation directed by: Professor Theodore L. Einstein
                             Department of Physics

Organic thin films are central to many cutting-edge electronic devices. Improving our understanding of the characteristics of thin films is important not only to the development of condensed matter physics but also to our ability to engineer specialized devices that we demand be ever smaller, less expensive, and more efficient. This thesis applies the experimental techniques of scanning tunneling microscopy and spectroscopy to the task of characterizing submonolayer thin films of two types: the organic semiconductor C_{60} on silicon oxide, and self-assembling porous networks of trimesic acid on graphite.

Capture zone analysis of the initial nucleation regime for C_{60} on ultrathin silicon oxide is reported. The critical nucleus size, reflecting the largest unstable cluster of particles on a surface, is found to have a parabolic dependence on temperature rather than a monotonically increasing one. Between stages of stable monomers ($i = 0$) at < 300 K and > 480K, a peak corresponding to $i = 1$ is found at 386 ± 3 K. This unique temperature dependence is attributed to defect-like variation in the

silicon oxide surface.

The first successful room-temperature UHV STM of trimesic acid on graphite is also presented here. These exploratory studies indicate the potential for a variety of porous hexagonal networks of trimesic acid to exist on a graphitic surface at room temperature. Significant electronic effects on graphite from trimesic acid lattices are shown via scanning tunneling spectroscopy, including an electronic state at -0.14 V that appears in networks whose pores are filled with excess TMA guest molecules. Ultimately, if the growth of TMA films could be extended to graphene, then the periodicity of electronegative oxygen atoms in molecules physisorbed on the graphene surface is predicted to provide a slight energy shift between the degenerate sublattices, opening a band gap. Promising directions for future research in these areas are also discussed.

ORGANIC MOLECULAR THIN FILMS ON DEVICE-RELEVANT SUBSTRATES

by

Michelle Anne Groce

Dissertation submitted to the Faculty of the Graduate School of the
University of Maryland, College Park in partial fulfillment
of the requirements for the degree of
Doctor of Philosophy
2013

Advisory Committee:
Professor Theodore L. Einstein, Chair/Advisor
Professor Ellen D. Williams
Dr. William G. Cullen
Professor Janice Reutt-Robey
Professor Michael S. Fuhrer

Acknowledgments

My first thanks are certainly due to my faculty advisors, Ellen Williams and Ted Einstein. I am grateful to Ellen for welcoming me into the Surface Physics group at Maryland, helping me find my way to research projects that fit well with my aptitudes and interests in physics, and providing her superb insights during my first two and a half years in graduate school. I am also grateful to Ted for "adopting" me as his advisee when Ellen went on leave to BP, facilitating useful theory collaborations that both grounded and motivated my research, and encouraging me as I explored possibilities for my future career.

I have frequently described my grad school experience by saying that it takes a village to raise a PhD student; I next want to thank the rest of my "village"/thesis committee: Bill Cullen, Janice Reutt-Robey, and Michael Fuhrer. Bill, especially, has really been a co-advisor and direct supervisor of my experimental work. His vast expertise, keen troubleshooting instinct, and good-natured patience with me were absolutely invaluable.

The graduate students in this village of a research group were always friendly and supportive of me. There are too many to name everyone, but I want to specifically thank Brad Conrad, Jianhao Chen, Kristen Burson, and Mahito Yamamoto for being inspirational physicists and all-around awesome people. Postdoctoral researchers Yilin Wang and Veda Bharath were also wonderful colleagues who provided me with many useful insights about science and life in general.

Many of my favorite moments from graduate school are thanks to the phenom-

enal staff of the Maryland MRSEC, especially Donna Hammer, Julie Callis, and Alex Prasertchoung. I found the MRSEC's science education outreach programs to be very rewarding experiences, and I really appreciated the confidence that Donna, Julie, and Alex showed in me as a physics teacher. I would be remiss not to mention another significant part of my time here: coaching the Maryland Parliamentary Debate Society. It was a joy to work with this impressive group of students. I benefited from the break that debate provided in an otherwise all-physics routine, as well as from the earnest interest many debaters showed in my work. They took me up on my offers of lab tours, which helped me to clarify and refine my explanations (and understanding) of surface physics concepts.

Finally, I want to thank my family for their support throughout the entire past decade of my physics education. They have always believed in me even when I struggled to do so myself, and for that I am eternally grateful.

Table of Contents

v

List of Figures

List of Abbreviations

ARPES	angle-resolved photoemission spectroscopy
DFT	density functional theory
DOS	density of states
ΓD	gamma distribution
GWD	generalized Wigner distribution
HOMO	highest occupied molecular orbital
HOPG	highly-oriented pyrolytic graphite
KMC	kinetic Monte Carlo
LEED	low-energy electron diffraction
LUMO	lowest unoccupied molecular orbital
PVD	physical vapor deposition
STM	scanning tunneling microscopy/microscope
STS	scanning tunneling spectroscopy
TMA	trimesic acid, benzene-1,3,5-tricarboxylic acid
UHV	ultra-high vacuum
UTO	ultra-thin oxide

Chapter 1

Introduction

The field of surface and interface physics is concerned with situations in which one of the typical solid-state assumptions no longer applies; specifically, the crystals studied are not periodic in all three spatial dimensions, but rather are only two-dimensional—or, in the case of nanowires or step edges, effectively one-dimensional. This change in dimensionality can change the properties of a crystal significantly, even though the bulk material, monolayer, and nanowire are all made of the same constituent parts.

Understanding these changes is important in many contexts. A layered structure consisting of two or more bulk crystals could not be fully described without accounting for physical and electronic effects at the heterojunctions, the two-dimensional interfaces between layers. A material measurement made by an instrument probe, depending on the size of the probe and its proximity to the material, may require detailed characterization of the material and probe surfaces in order to be accurately interpreted. Moreover, with a better understanding of low-dimensional structures, we can engineer new materials with specific properties in mind and design nanoscale electronic devices from the bottom up.

In this thesis, I will present investigations of low-dimensional structures in order to better understand their unique electronic properties. These investigations
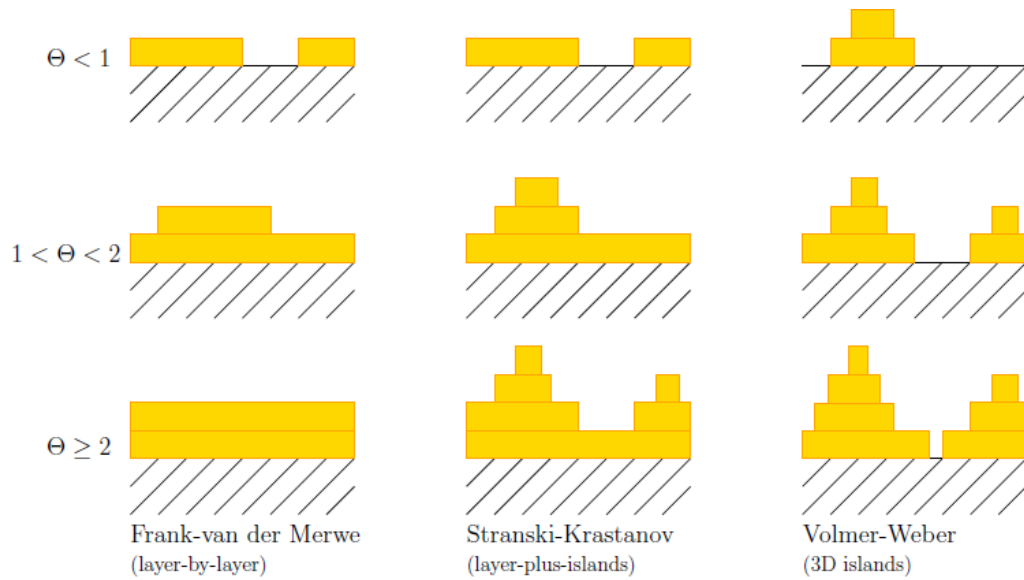
Figure 1.1: Primary growth modes of thin films.

are also motivated by a forward-looking interest in device engineering applications.

1.1 Thin film nucleation and growth

Thin film growth is a large area of study in the field of surface science [1, 2, 3]. In order to successfully and thoroughly characterize the initial nucleation processes and growth modes of a molecule on a given substrate, one must consider many phenomena. These include the influence of the substrate on a molecule's shape and charge distribution, the opposite effect of the molecules on the substrate, the intermolecular interactions, and the facilitation or constraint of molecular diffusion on the surface. Further effects, such as the influence of temperature or pressure on film growth, may also be explored. All this information contributes to our fundamental understanding of physics and chemistry of materials.

Of course, this basic research also comes with practical applications. Thin film organic electronic devices, such as photovoltaic cells, light-emitting diodes, and field-effect transistors, are known to be significantly impacted by film morphology and detailed molecular order [4, 5, 6]. Therefore, by charting the parameter space of fabrication conditions that can affect film growth modes (Fig. 1.1) and resulting morphology, surface scientists enable customization of organic electronic films.

To appreciate the impact of such research, it is instructive to consider the case of organic thin-film photovoltaics. Typically composed of an electron-donor material and electron-acceptor material sandwiched between electrodes, their performance is heavily dependent on the donor-acceptor interface where exciton separation occurs. Two distinct, planar crystals (such as those formed in layer-by-layer growth) create a minimum interfacial area, but the separation efficiency can be improved by increasing that area as in Figure 1.2a. Results of more realistic fabrication procedures generally look more like the bulk heterojunction illustrated in Figure 1.2b, which does result in a larger interface between materials but also includes regions which are completely isolated from their associated electrode. Carriers may become trapped in these islands, reducing PV efficiency. Optimizing the balance between these two effects requires thorough investigation and measurement of the film growth process.

In one example of such an investigation, Salzmann *et al.* [8] applied a variety of techniques to measure pentacene/C_{60} heterostructures on a conductive polymer substrate. Codeposition of both molecules produced photovoltaic devices that were less efficient than sequential deposition into planar structures, so the authors experimented with both techniques, adding pentacene pre-covering and post-deposition

Ideal

Anode

Donor

less than
10 nm

Acceptor

Cathode

(a)

Realistic
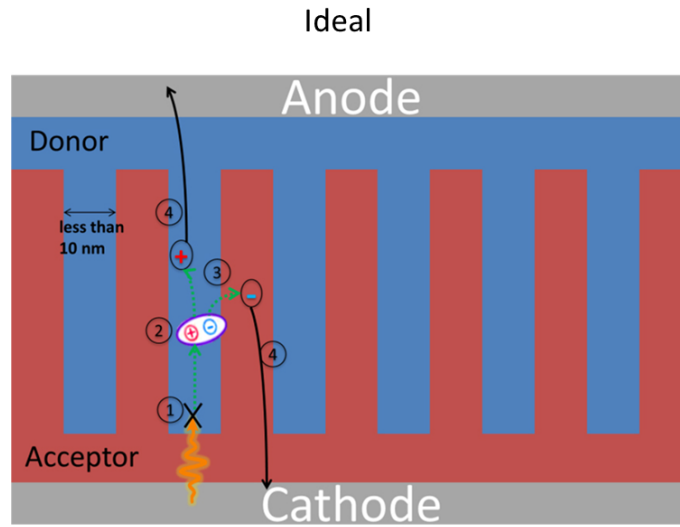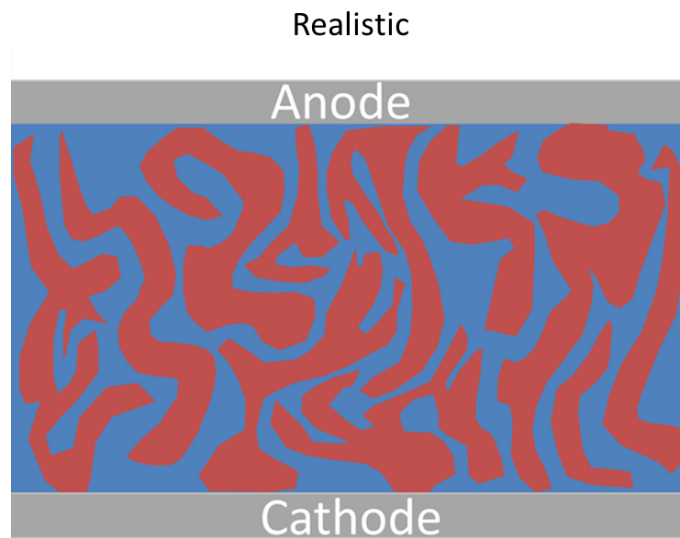
Anode

Cathode

(b)

Figure 1.2: (a) An idealized schematic of an organic thin film photovoltaic cell. Incoming radiation (1) creates an exciton (2) which separates at the donor-acceptor interface (3). The separated electron and hole travel (4) to the cathode and anode, respectively. (b) A dispersed heterojunction of donor and acceptor molecules. Interfacial surface area is greatly increased over a planar structure, but some regions are isolated from the electrodes and will trap diffusing carriers. Illustration respectfully borrowed from [7].
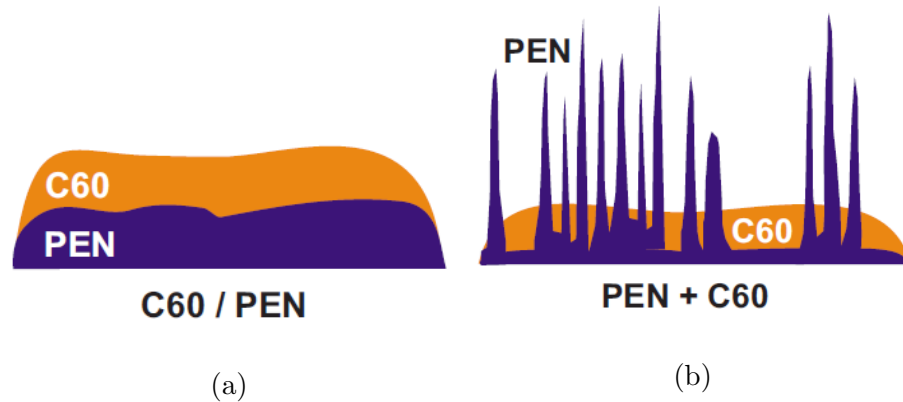
Figure 1.3: Schematic models of films experimentally measured in [8]. (a) Layered growth of C_{60} on pentacene, deposited sequentially. (b) Codeposition of pentacene and C_{60} on top of a previously-deposited pentacene underlayer. Illustration respectfully borrowed from [8].

annealing. By measuring the HOMO-LUMO level offset, film crystallinity, and overall surface morphology, they found that in codeposited films pentacene phase-separated into needle-like islands more than an order of magnitude taller than the surrounding C_{60}, meaning that pentacene crystallites would contact both electrodes in an OPV cell and facilitate current leakage. The authors recommend controlling deposition flux rate and substrate temperature during growth in order to adjust this structure (illustrated in Fig. 1.3b) closer to that of Fig. 1.2a.

From a basic research standpoint, there are naturally many other questions to be asked and answered beyond addressing these engineering challenges. What specifically governs the process by which a gas of particles becomes a crystal? Is there a meaningful distinction to be made between a "nucleus" of particles accumulating on a surface and a "grain" in a film, and if so, what causes the transition from one to the other? In order to tackle these questions in a scientific and quantitative

5

way, the *critical nucleus size* was defined [9]. Now commonly referred to with the variable i, the critical nucleus size denotes the number of particles in the largest unstable cluster on a surface. At or below i, that cluster is at least as likely to break apart as it is to remain together. Once one additional particle is added, the cluster becomes more likely to remain together than break apart, and is expected to grow into an island. Thus, $i = 0$ refers to the case of stable monomers, $i = 1$ to stable dimers, and so on.

Although it was initially defined and understood to be restricted to integer values [10], more recent interpretations of the critical nucleus size have allowed it to take any nonnegative real value, considering a noninteger i as a reflection of the detachment probability of a quasi-stable cluster of $i + 1$ atoms [11]. Decades of work have been done to understand the nucleation and growth process in terms of i, developing models to extract it from (or predict it for) various material systems, and applying it to the optimization of film growth procedures. Adsorbate/surface pairings with smaller values of i produce more corrugated films with a smaller grain size, while larger values of i lead to films with larger single-crystalline regions [12]. Further discussion of these models and calculation methods can be found in Chapter 3, in addition to their application to the case of C_{60} nucleation on SiO_2.

1.2   Electronic properties of graphene

Another rich area in the field of surface physics encompasses graphene and its many remarkable properties [13]. Graphene is an all-surface material, a two-
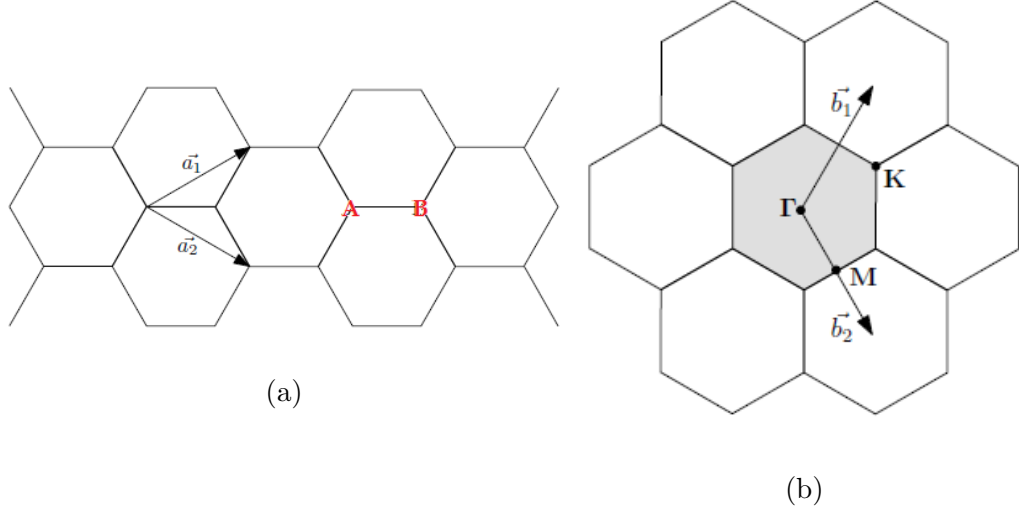
Figure 1.4: (a) Graphene lattice in real space, with carbon atoms located at vertices. The primitive lattice of graphene is described by $\vec{a}_1$ and $\vec{a}_2$ with a two-atom basis labeled by A and B. (b) Graphene lattice in reciprocal (momentum) space. The first Brillouin zone is shaded in gray and points of high symmetry are marked.

dimensional honeycomb lattice consisting of sp^2-bonded carbon atoms. The honeycomb lattice is not a Bravais lattice; rather, it is made up of two interlaced, identical hexagonal lattices. This may also be described as a two-atom basis in a hexagonal lattice (see Fig. 1.4a) with unit vectors given by

$$\vec{a_1} = a_0\frac{\sqrt{3}}{2}\hat{x} + \frac{a_0}{2}\hat{y} \tag{1.1}$$
$$\vec{a_2} = a_0\frac{\sqrt{3}}{2}\hat{x} - \frac{a_0}{2}\hat{y}$$

where a_0, the graphene lattice constant, is approximately 2.46Å.

The allowed energy levels for carriers within graphene can be calculated effectively using the tight binding approximation [14, 15]. The energy bands are expressed in terms of the wavevector $\vec{k}$, so it is necessary first to transform the

7

lattice into momentum space. The reciprocal lattice is described by the unit vectors

$$\vec{b_i} = 2\pi \frac{\vec{a_j} \times \vec{a_k}}{\vec{a_1} \cdot (\vec{a_2} \times \vec{a_3})} \tag{1.2}$$

using Eqs. (1.1) and $\vec{a_3} = \lim_{c \to \infty} c\hat{z}$. This formula gives a two-dimensional lattice of

$$\vec{b_1} = \frac{2\pi}{a_0\sqrt{3}}\hat{x} + \frac{2\pi}{a_0}\hat{y} \tag{1.3}$$

$$\vec{b_2} = \frac{2\pi}{a_0\sqrt{3}}\hat{x} - \frac{2\pi}{a_0}\hat{y}$$

The points of high symmetry in the Brillouin zone defined by these vectors, illustrated in Figure 1.4b, are the Γ point at the center, the K point at the corner, and the M point in the middle of the edge.

Applying the tight binding model amounts to solving the secular equation $\det[\mathcal{H} - E\mathcal{S}] = 0$, where $\mathcal{H}_{ij} = \langle \Psi_i | \mathcal{H} | \Psi_j \rangle$ is the Hamiltonian matrix and $\mathcal{S}_{ij} = \langle \Psi_i | \Psi_j \rangle$ is the overlap matrix for atomic wavefunctions Φ_i. For graphene, in a first approximation, this model is applied to the π orbitals perpendicular to the plane, and the system is restricted to nearest-neighbor interactions. Thus, the matrices $\mathcal{H}$ and $\mathcal{S}$ describe carrier hopping between the $2p$ states of A and B atoms in the lattice. $\mathcal{H}_{AA}$ and $\mathcal{H}_{BB}$ are both simply equal to E_{2p}, the energy level of the $2p$ orbital at one site. $\mathcal{H}_{AB}$ and $\mathcal{H}_{BA}$ must take into account the phase factors arising in Bloch wavefunctions through a translation from one site to each of its three nearest neighbors. Hopping from A to B, as in Fig. 1.4a, would correspond to

translations $\vec{R}_1 = \frac{a_0}{\sqrt{3}}\hat{x}$, $\vec{R}_2 = -\frac{a_0}{2\sqrt{3}}\hat{x} + \frac{a_0}{2}\hat{y}$, and $\vec{R}_3 = -\frac{a_0}{2\sqrt{3}}\hat{x} - \frac{a_0}{2}\hat{y}$; thus,

$$
\begin{aligned}
\mathcal{H}_{AB} &= -t\left(e^{i\vec{k}\cdot\vec{R}_1} + e^{i\vec{k}\cdot\vec{R}_2} + e^{i\vec{k}\cdot\vec{R}_3}\right) \\
&= -t\left(e^{ik_xa_0/\sqrt{3}} + e^{-ik_xa_0/2\sqrt{3}-ik_ya_0/2} + e^{-ik_xa_0/2\sqrt{3}+ik_ya_0/2}\right) \\
&= -t\left(e^{ik_xa_0/\sqrt{3}} + 2e^{-ik_xa_0/2\sqrt{3}}\cos\frac{k_ya_0}{2}\right)
\end{aligned}
\tag{1.4}
$$

The transfer integral t is the energy of nearest-neighbor hopping, $\langle\phi_a|\mathcal{H}|\phi_B\rangle = \langle\phi_B|\mathcal{H}|\phi_A\rangle$, which is typically given as 3.033 eV [14, 15].

The overlap matrix $\mathcal{S}$ is much simpler, since the wavefunctions can be assumed to be normalized as well as localized under the Slater-Koster scheme [15] which results in $\mathcal{S} = \mathbb{1}$. Solving $\det[\mathcal{H} - E\mathcal{S}] = 0$ gives the energy dispersion relation

$$
E(\vec{k}) = \pm t\left[1 + 4\cos\left(\frac{\sqrt{3}}{2}a_0k_x\right)\cos\left(\frac{a_0k_y}{2}\right) + 4\cos^2\left(\frac{a_0k_y}{2}\right)\right]^{1/2}
\tag{1.5}
$$

plotted in Figure 1.5a. The energy E_{2p} has been set to zero for clarity, since the two branches of the dispersion relation are symmetric around that value.

Of particular interest are the Dirac cones around each K point in the Brillouin zone, where the valence and conduction bands come together at a point. This is a direct result of the fact that $\mathcal{H}_{AA} = \mathcal{H}_{BB}$. If the energies at the A and B lattice sites were slightly different—in other words, if the energy degeneracy were broken between the sublattices—the bands would be separated by a gap, turning the crystal into a semiconductor (Figs. 1.5b and 1.5d). I show this by following the same tight binding calculations as above [14, 15] while letting $\mathcal{H}_{AA} = E_1$ and $\mathcal{H}_{BB} = E_2$ and defining $2\Delta = |E_1 - E_2|$ and $E_{\text{ave}} = (E_1 + E_2)/2$ (and noting that t would have a

(a)

(b)

(c)

(d)

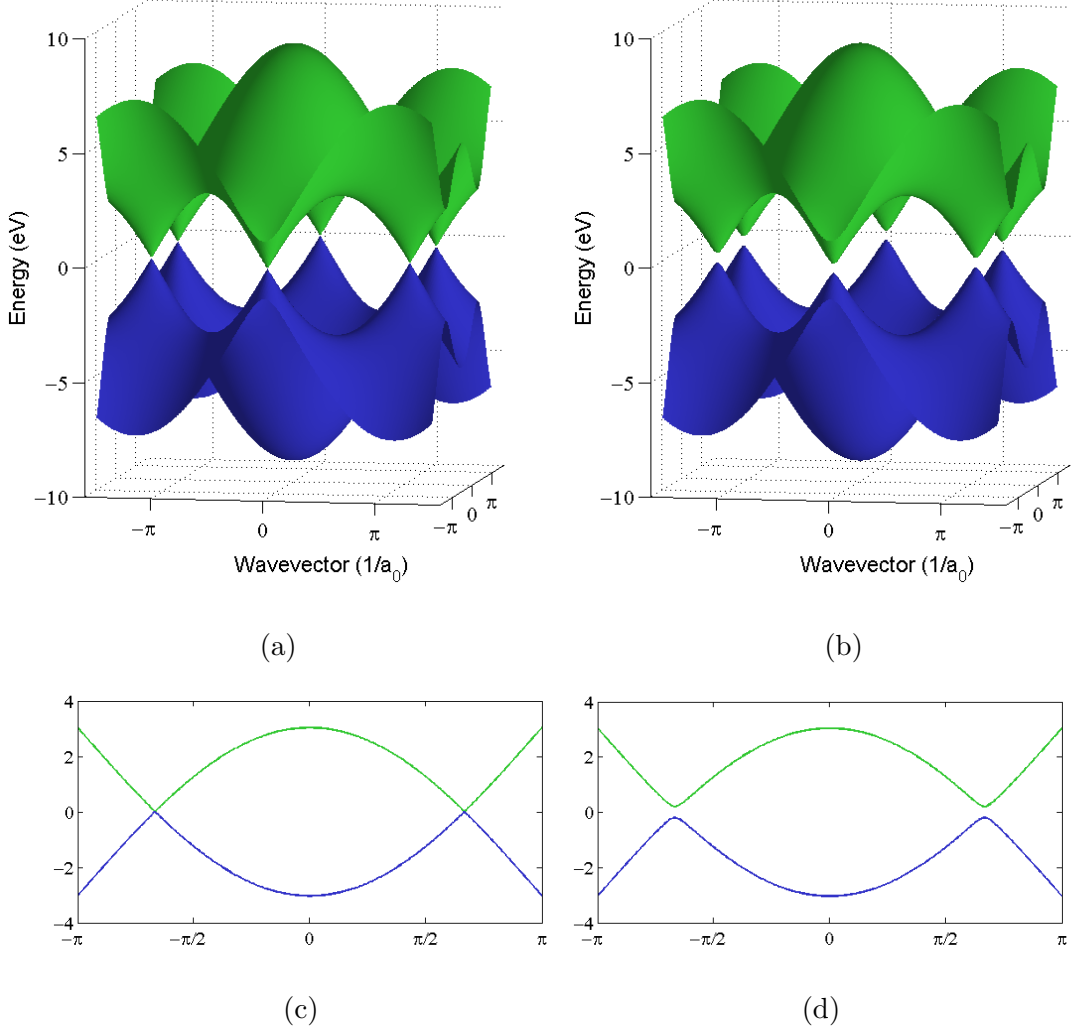Figure 1.5: (a, b) Dispersion relation $E(\vec{k})$ for pristine graphene follow-
ing Eq. (1.5) and for symmetry-broken graphene following Eq. (1.6)
and leaving the value of t unchanged. The upper, green surface is the
conduction band and the lower, blue surface is the valence band. (c,d)
Cross-section of $E(\vec{k})$ for pristine and symmetry-broken graphene show-
ing $E(k_y)$ for $k_x = 2\pi/a_0\sqrt{3}$.

slightly different, but still constant, value). One can then write $\det[\mathcal{H} - E\mathcal{S}] = 0$ as

$$(E_{\text{ave}} - \Delta - E)(E_{\text{ave}} + \Delta - E) - t^2 \left(1 + 4\cos\frac{\sqrt{3}}{2}a_0k_x \cos\frac{a_0k_y}{2} + 4\cos^2\frac{a_0k_y}{2} \right) = 0$$

$$(E_{\text{ave}} - E)^2 - \Delta^2 - t^2 \left(1 + 4\cos\frac{\sqrt{3}}{2}a_0k_x \cos\frac{a_0k_y}{2} + 4\cos^2\frac{a_0k_y}{2} \right) = 0$$

Setting $E_{\text{ave}} = 0$ as with E_{2p} in the previous configuration,

$$E(\vec{k}) = \pm \left(\Delta^2 + t^2 \left(1 + 4\cos\frac{\sqrt{3}}{2}a_0k_x \cos\frac{a_0k_y}{2} + 4\cos^2\frac{a_0k_y}{2} \right) \right)^{1/2} \tag{1.6}$$

which is plotted in Figures 1.5b and 1.5d. The width of the resulting energy gap is simply 2Δ.

1.2.1   Symmetry-breaking via substrate composition

Varying the substrate composition has been investigated as a potential method for breaking the *A-B* sublattice degeneracy in graphene. If a graphene sheet is deposited or grown on a surface that has a periodic modulation in electronic or topographic structure, local changes in the graphene may be effected. If the substrate has a periodicity different from that of graphene's primitive lattice, a semiconducting gap may be opened.

Zhou *et al.* [16] observe this semiconducting gap in graphene grown epitaxially on silicon carbide. Using angle-resolved photoemission spectroscopy (ARPES), they demonstrate a gap of ~ 0.26 eV at the K point in single-layer samples. As more graphene layers are added, the gap width smoothly and monotonically approaches zero. Extrapolating from data on single-, bi-, and trilayer graphene,[1] the authors

---

[1] The terms "multi-layer graphene" and "few-layer graphite" are each sometimes used to refer

argue that 5 layers is the minimum necessary for the band gap to close and reveal the familiar Dirac cone. They attribute the single-layer gap to symmetry-breaking interactions between graphene and the SiC buffer layer. A similar trend in increasing layers of epitaxial graphene on SiC has also been found using scanning tunneling spectroscopy [17, 18].

In fact, one might reasonably expect [19] that bilayer graphene would be more likely to show a gap than single-layer graphene—analogous to placing a graphene sheet on a graphene substrate. The second layer is offset from the one below it so that one sublattice is situated in hollow sites above the center of rings and the other is atop carbon atoms from the first layer, and this interlayer coupling should break the A-B energy degeneracy. Symmetry-breaking has been inferred from quantum Hall measurements of suspended bilayer graphene [20], but results for bilayer samples on substrates are dependent on the nature of the substrate's electronic influence. A band gap is present in bilayer graphene on SiC [21] but not on SiO_2 [22]. However, both theoretical [23] and experimental works have confirmed that in bilayer graphene a tunable semiconducting gap of up to ~ 300 meV can be created by introducing a potential difference between the graphene layers, either through doping (as in [21]) or through application of an external electric field (as in [22]), paving the way for dual-gated bilayer graphene devices.

to materials with a relatively small number of stacked atomic layers of carbon. The choice to call this "graphene" or "graphite" largely depends on the emphasis of one's own research. For clarity, in this thesis, I will use expressions of the form "n-layer graphene" when an exact value of $n < 10$ is known.

Another approach to graphene symmetry-breaking is to induce strain. This distorts the C-C bond lengths, changing the transfer integral along different crystallographic directions. Graphene can be deposited on flexible substrates and then stretched without breaking [24], but uniaxial strain must be impractically large (over 26.5%, in the zigzag direction) in order to create a band gap [25, 26]. Tight binding calculations of graphene under both uniaxial and shear strain predict a tunable band gap up to 900 meV without risking structural failure [27]. Several groups are exploring creative solutions for engineering more complex strain patterns experimentally [28, 29].

Substrate crystals providing close registry with the graphene lattice have also been considered. Giovannetti *et al.* [30] report their *ab initio* calculation of graphene band structure on four layers of lattice-matched hexagonal boron nitride. hBN has a structure very similar to that of graphene with a lattice mismatch of less than 2%; the two sublattices are of course nonidentical, being made of boron and nitrogen atoms. Since the two atoms in the graphene unit cell are positioned above different regions of the BN cell, their local energy levels are altered (see Fig. 1.6). They calculate the lowest-energy configuration to be that with one carbon atom above the center of a BN honeycomb ring and the other carbon atom atop boron. This results in a band gap of 53 meV at the K point.

This exact structure is, at least at present, prohibitively difficult to create experimentally. Nevertheless, other new and interesting physical phenomena have recently been observed in graphene in a twisted alignment on an hBN substrate [31, 32, 33, 34], including the emergence of a varying-width band gap of tens of meV

13
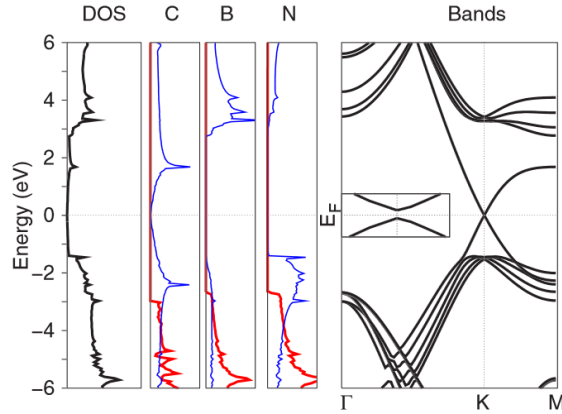
Figure 1.6: DFT calculations of graphene atop hexagonal boron nitride, showing (from left to right): total density of states; carbon, boron, and nitrogen projected density of states in-plane (red) and out-of-plane (blue); band structure around the K point. A magnified inset shows a 53 meV gap. Respectfully borrowed from Ref. [30], Figure 3.

scaling with the Moiré wavelength [33]. This system will certainly see continued research. It was also strongly suggestive of the approach discussed in the following section.

1.2.2 Symmetry-breaking via adsorbed molecules

Substrate-engineering has produced many interesting results, despite being a new area even within the young field of graphene research. These studies also lend credence to the idea that placing a periodic structure against a graphene sheet could break the A-B sublattice degeneracy, inspiring another area of parallel investigation. Instead of putting that structure beneath the graphene, it appears to be possible to engineer symmetry-breaking by adsorbing an ordered lattice of molecules on top of a graphene sheet. The "right" choice of molecule, with appropriate order in the molecular layer and strength of molecule-graphene interaction, could introduce

local shifts in electronic energy levels and open a band gap. If the molecular layer spontaneously self-assembles on the surface, this approach would amount to a simple surface coating on graphene devices already fabricated by established procedures, and therefore could easily be integrated in industrial applications.

Many different molecular species have been considered for these adsorbate studies. For the purposes of this thesis I classify these molecules into two main groups. The first is composed of strong symmetry-breakers, small molecules that interact repulsively to form triangular lattices approximately the same size as the graphene unit cell. A great deal of chemistry research using calorimetry, x-ray diffraction, and reflection-absorption infrared spectroscopy has been done with small dipolar halocarbons such as CF_3H, CF_3Cl, and others on the basal plane of graphite [35, 36, 37, 38]. Adsorption of these molecules has recently been observed to affect graphene's transport properties with potential for chemical sensor applications [39]. However, the films are typically only stable at low temperatures ($<$ 150 K). A gapped-graphene transistor would ideally be operational at room temperature or higher (*e.g.*, in computer processors).

The second group of potential adsorbates is the weak symmetry-breakers, larger aromatics that form two-dimensional hydrogen-bonded lattices with period-icities several times the size of graphene's. Density functional theory has been used to predict energetically favorable orientations, and the resulting charge transfer, for various molecules of this sort physisorbed on graphene [40, 41]. H-bonding between the molecules creates stable long-range order that has the potential to repeat that charge transfer at regular intervals in registry with the graphene. For that reason,

in this work I focus on this second group of molecules, and in particular benzene-1,3,5-tricarboxylic acid ($C_9H_6O_6$), commonly referred to as trimesic acid or TMA. The molecule's central six-carbon ring is functionalized by carboxyl groups at alternating sites; that is, supposing we begin with a benzene molecule, at every other carbon in the ring a bonded hydrogen atom is replaced by another carbon, which is in turn double-bonded to one oxygen atom and single-bonded to an OH group.

The bulk structure of trimesic acid, described in [42], is composed of a "chicken-wire motif," a honeycomb-like structure in which each ring is formed by six molecules hydrogen-bonded at the carboxyl groups. The three-dimensional crystal consists of different honeycombs interlocking through their pores. Two-dimensional versions of similar motifs have been observed using scanning tunneling microscopy (STM) of TMA films formed by physical vapor deposition [43, 44, 45] or in droplets of a TMA solution [46, 47, 48, 49].

Ref. [44] demonstrated that increasing coverage of TMA on Au(111) forms increasingly dense hexagonal porous networks, as shown in Figure 1.7. The basic structure, with two (2×1) TMA molecules in its unit cell, corresponds to the honeycomb motif and is labeled H_{TMA-1} (shortened in this work to H_1). The next structure in increasing density has a unit cell six $(2 \times (1+2))$ molecules and forms a "flower" motif; this is labeled H_2. H_3 has twelve $(2 \times (1+2+3))$ molecules, H_4 has 20 molecules, and so on. The TMA molecule and the first three hexagonal networks are illustrated in Figure 1.8. All these networks' unit cells are very close to integer multiples of the graphene unit cell, suggesting a high likelihood of excellent registry.

A large body of work has been done on the self-assembly of TMA and re-
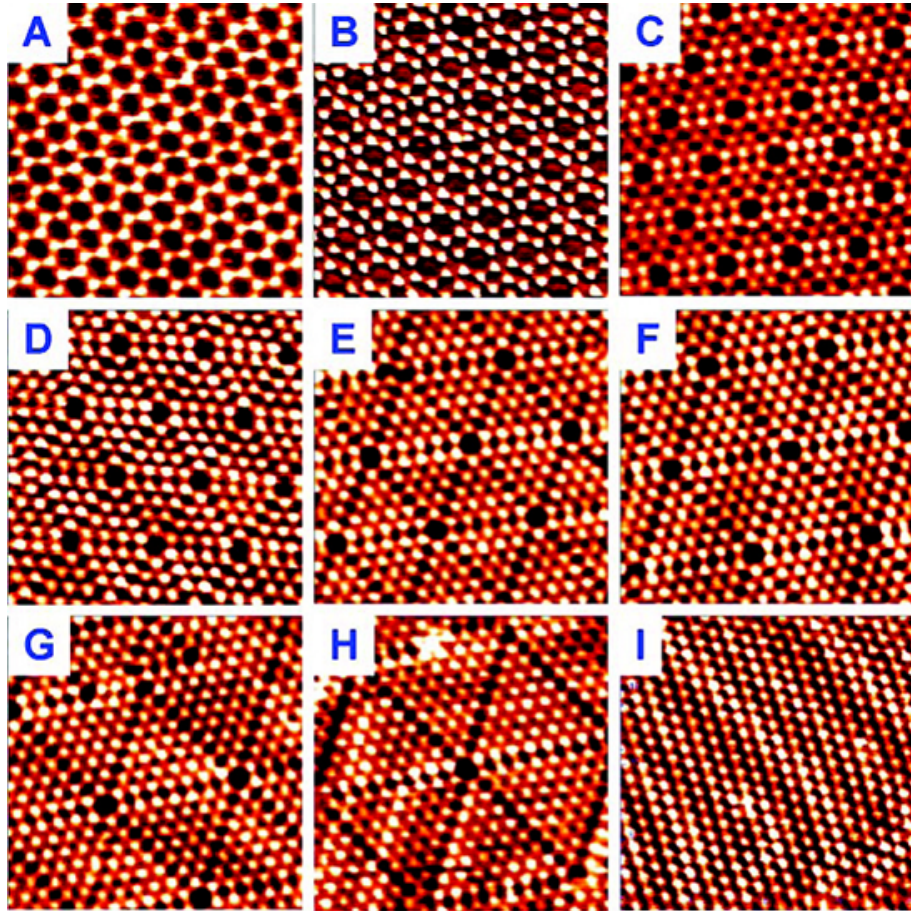
Figure 1.7: Increasing the deposition coverage of TMA on Au(111) forms increasingly dense hexagonal porous networks, from H_1 in the upper left STM image, to H_∞ in the lower right. Respectfully borrowed from [44].

(a)

(b)

(c)

(d)
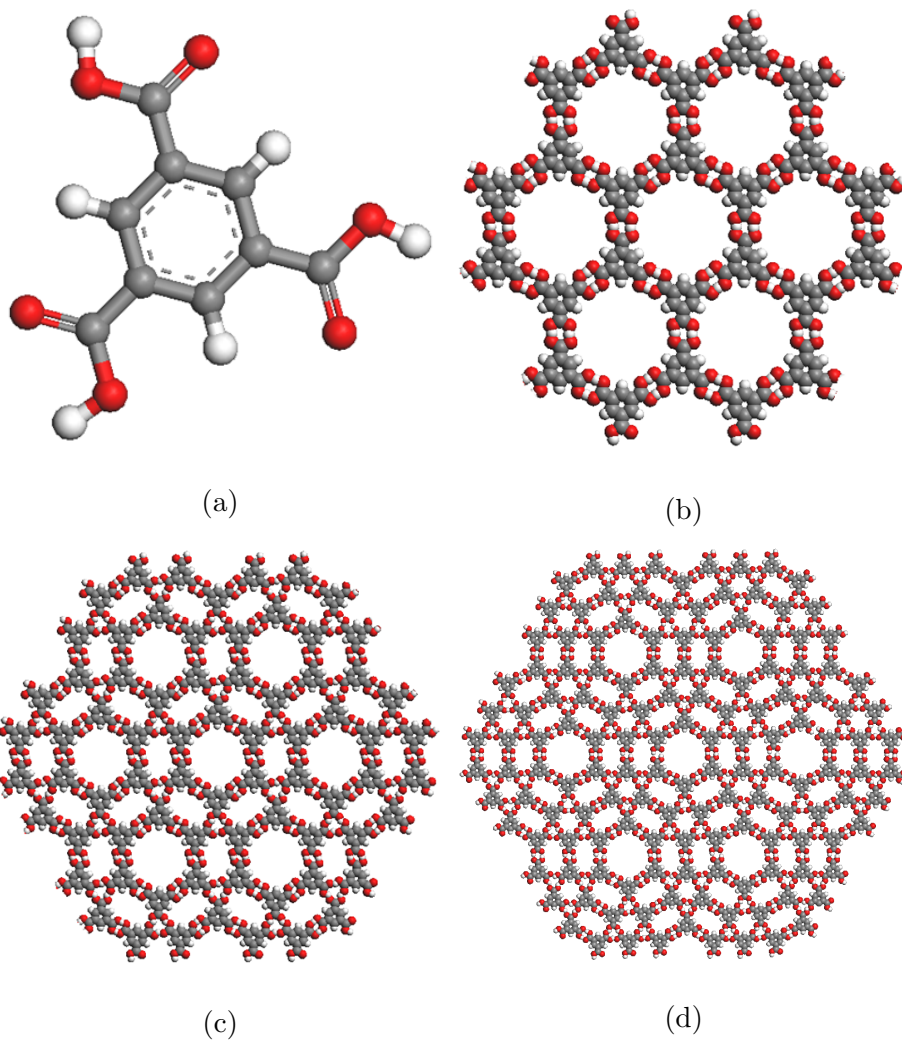
Figure 1.8: Trimesic acid structures. Gray spheres denote carbon, red corresponds to oxygen, and white is hydrogen. (a) A single TMA molecule. (b) H_1 phase, also labeled "honeycomb" or "chicken-wire." (c) H_2 phase, also labeled "flower." (d) H_3 phase.

18

(a)   (b)
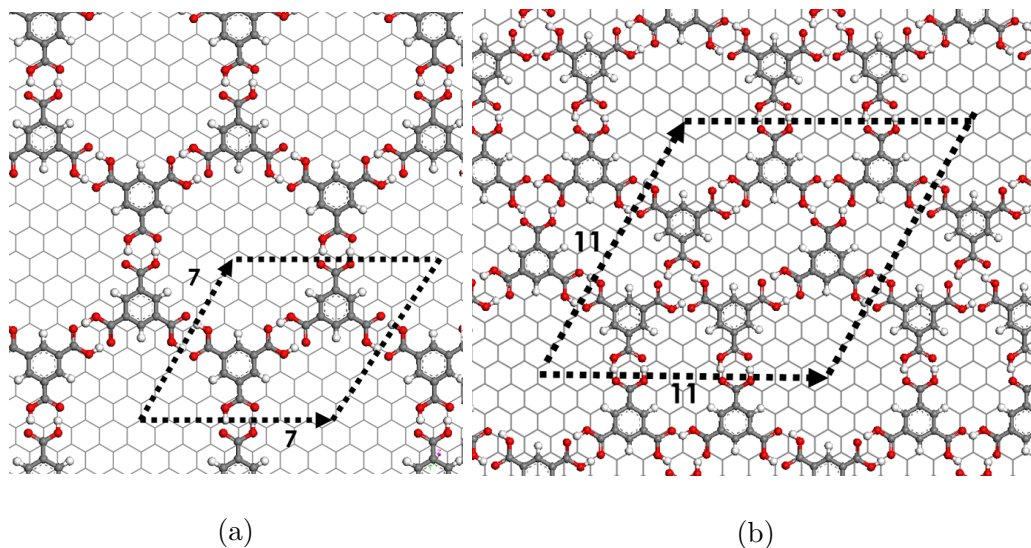
Figure 1.9: Symmetry-breaking configurations of TMA phases H_1 (honeycomb) and H_2 (flower). The oxygen atoms, in red, always sit atop one graphene sublattice and never the other.

lated molecular networks on graphite and graphene. Several studies have observed H_1 and H_2 rotated 4-6° to the HOPG(0001) surface whether in solution or UHV [49, 50]. A variety of porous structures have been created through coadsorption of TMA with other aromatic molecules varying ratios [49, 45]. Density functional theory calculations of benzene derivatives on graphene have been performed; specifically, comparison of benzoic acid (C_6H_5COOH), terephthalic acid ($C_6H_4(COOH)_2$ or TPA), and TMA showed increased binding to graphene with increased number of carboxyl groups [51]. Other research has focused on TMA and TPA grain boundary dynamics [47] and the mass transport of "guest" molecules hopping from pore to pore [52].

However, little work has as yet been done to quantify the effects of these molecular networks on substrate electronic energy levels. Indications of symmetry-

breaking were observed in Raman spectra of graphene chemically exfoliated in a TPA solution [53]. Ref. [51] only speculated about large-scale ordered networks of molecules, but found that in a single molecule on graphene the TMA HOMO is localized near the oxygen atoms while the LUMO is delocalized. Given the expected close registry of TMA monolayers with a graphene sheet, this indicates a promising mechanism for symmetry-breaking. Phases in which oxygen atoms are situated above only one sublattice of graphene (Fig. 1.9) should cause a shift in energy levels throughout that sublattice, opening a gap. These structures will be further discussed in Chapter 4.

1.3 Outline of this thesis

The remainder of this work will elaborate on my own experimental investigations into organic molecular thin films. Chapter 2 contains explanations of measurement methods, primarily scanning tunneling microscopy and spectroscopy, and procedures for sample preparation. Chapter 3 describes my investigation of the initial nucleation stages of C_{60} films grown on silicon oxide. My studies of trimesic acid on HOPG are detailed in Chapters 4 and 5, the former focusing on structural phases observed by STM, and the latter detailing STS measurements of local density of states.

Chapter 2

Experimental methods

Binnig and Rohrer's 1982 invention of the scanning tunneling microscope was quickly recognized as revolutionary by the physics community, which awarded them the Nobel Prize for it only four years later [54]. The STM was unlike many other, older surface measurement techniques in that it provided a real-space image of atomic structure. It also enabled local spectroscopy of materials' electronic state densities. Thirty years after its invention, the STM is a staple of surface science research.

Given that STM technology has advanced so far over the past decades and that commercially-designed microscopes are now at least as common as those custom-built in research labs, it is not necessary to explain all the principles behind the technique. Instead, I will discuss a few essential points of the mechanisms underlying STM and STS and explain the particulars of the ultra-high vacuum system and sample preparation techniques that were used for the experiments in this thesis.

2.1   Scanning tunneling microscopy

STM harnesses the principle of quantum tunneling to obtain high-resolution images of conducting or semiconducting surfaces. By bringing a sharp metal tip within Angstroms of a sample surface and applying a voltage between the two,

electrons in one have a small but nonzero probability to tunnel through the empty region—typically vacuum or air—into the other.

In a low-voltage approximation [55, 56, 57], the tunneling current is related to the size of the gap by

$$I \propto \frac{V}{d} e^{-A\bar{\phi}^{1/2}d} \tag{2.1}$$

where V is the bias voltage applied between the tip and the sample, d is the physical distance between them, $A = 1.025(\text{eV})^{1/2}\text{Å}^{-1}$ and $\bar{\phi}$ is the average potential barrier height. This can be interpreted as an analog to Ohm's law $V = IR$ (with an exponential decay factor) where the distance d plays the role of the resistance.

The low-voltage approximation is not valid for tunneling on semiconductors, which can require biases of several volts. In these cases, it is more accurate [57, 58] to write

$$I \propto \int_0^{eV} \rho_S(E) D(E, V) dE \tag{2.2}$$

where ρ_S is the sample density of states and D is the barrier transmission coefficient. Applying the WKB approximation to describe D [57] yields the expression

$$I \propto \int_0^{eV} \rho_S(E) \rho_T(E) T(E, V) dE \tag{2.3}$$

with the tunneling probability T given by

$$T = \exp\left(-\frac{2d\sqrt{2m}}{\hbar} \sqrt{\bar{\phi} + \frac{eV}{2} - E}\right) \tag{2.4}$$

With this expression it is readily apparent that the tunneling current depends on the vertical distance between tip and sample as well as the local sample conductivity.

Topographic images of a surface are obtained by fixing a constant current setpoint and scanning the tip across a pre-set area of the surface. A feedback loop

22
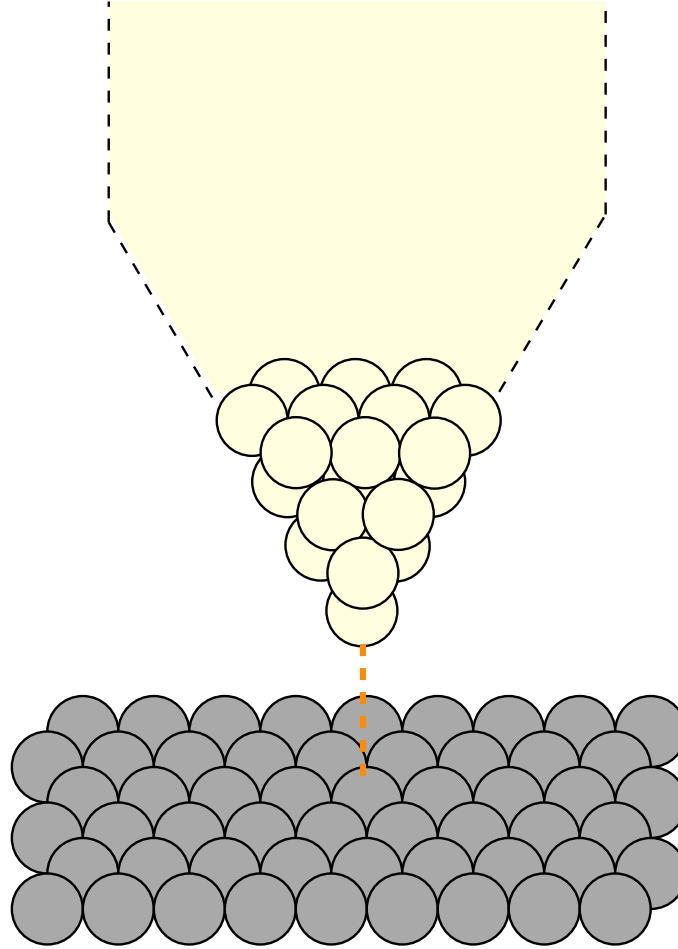
Figure 2.1: Schematic of tip-sample tunneling. In the ideal picture, the tunneling tip has a single atom at its point, which is brought within several Angstroms of the sample surface.

adjusts the tip height z in order to maintain the desired current value. These adjustments are then mapped to an image in which, typically, bright regions correspond to taller/more conductive features and dark regions correspond to lower/less conductive ones.

2.2 I-V spectroscopy

The same mechanism that allows the creation of topographic images can also be used to probe the substrate energy levels directly. Fixing the tip's position and sweeping the bias voltage causes a variation in tunneling current related to the sample density of states [58]. Specifically, Equation (2.3) can be differentiated with respect to V:

$$\frac{dI}{dV} \propto \rho_S(eV)\rho_T(eV)T(eV,V) + \int_0^{eV} \rho_S(E)\rho_T(E)\frac{dT(E,V)}{dV}dE \qquad (2.5)$$

Since T is expected to be smooth and monotonic, and ρ_T is typically assumed to be constant in the region of interest, the primary contributor to differential changes in tunneling current is the sample DOS. As voltage range or tip-sample distance is increased, the proportionality of dI/dV to ρ_S may be overshadowed, but this can be largely corrected for by computing $(dI/dV)/(I/V)$ instead [58]. Thermal noise and, somewhat ironically, an excessively sharp tunneling tip [57] can also degrade the resolution of STS data. However, Figure 2.2 provides a fair approximation of the spectroscopy process, and features observed in dI/dV are interpreted as features in ρ_S with these caveats.

One particularly useful application of scanning tunneling spectroscopy involves acquiring I-V spectra above specific locations in the surface [59]. Whether at single points, over a line across a region of interest, or in a grid over a larger region, this technique allows electronic features of substrate to be correlated with particular physical features.
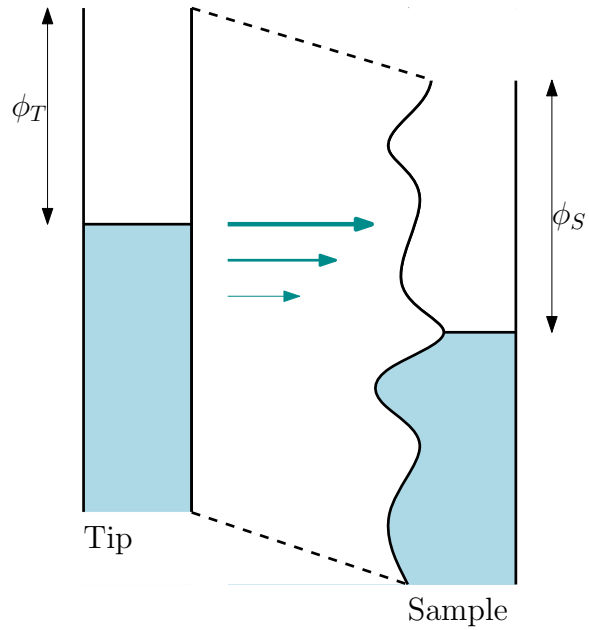
Figure 2.2: Illustration of spectroscopic determination of local density of states. Shown here, a positive bias on the sample relative to the tip results in electron tunneling from tip to sample. The tunneling rate is proportional to the unoccupied states in the sample accessible from tip electron energies. With bias reversed, tunneling from sample to tip is proportional to filled sample states. The sample DOS is extrapolated from the differential tunneling current as a function of bias voltage.

2.3 The Omicron VT-STM system

The experimental results discussed in this thesis were obtained using the Omicron VT-STM system located in the Surface Physics Group at the University of Maryland. This system consists of several distinct parts, integrated within a custom stainless steel ultra-high vacuum setup.

Principal among these parts is a variable-temperature, commercial STM (Omicron NanoTechnology GmbH) located in chamber A in Figure 2.3. The Omicron VT-STM allows for STM measurements at room temperature as well as low temperature (sample $T \geq 50$ K) through a flow cryostat or high temperature ($T \leq 1200$ K) via resistive heating, either of sample materials directly or of a pyrolytic boron nitride (PBN) heating element mounted underneath the sample. In this thesis, the STM was operated at room temperature. Liquid helium flow temperature operation was also briefly explored, but did not yield usable data. The Omicron scan head is configured to allow coarse x-y positioning of the tip relative to the sample over several millimeters. Finer positioning within $15{\times}15$ μm^2 was achieved using Nanonis software control of the piezoelectric scan tube.

Adjacent to the STM chamber is a large transfer chamber, denoted by B in Figure 2.3. The base pressure in the connected volume of A and B is $< 5 \times 10^{-11}$ Torr. This in turn connects to chamber C, a load lock which also includes a Knudsen cell evaporator (D) for physical vapor deposition and a crystal monitor (E) for deposition flux measurement and calibration. The load lock is directly pumped on by a turbomolecular vacuum pump but can be sealed off by a gate valve. Another

valve connects the load lock volume to a gas manifold. A final valve (F) connects the load lock to the transfer chamber.

On the transfer chamber, several more PVD sources may be mounted (G) such that they point to a central axis. A manipulator arm (H) can be extended along this axis and rotated 360° as well as adjusted vertically or horizontally by ~ 2 cm. This allows samples to be positioned directly in front of any of these sources, and to be retrieved from the load lock or moved to the STM. A carousel (I) that can store up to six samples or STM tips is also located in this chamber. Low-energy electron diffraction (LEED) optics are mounted on top (J) so the crystallinity of an upward-facing sample can be measured.

Returning to chamber A, the STM sample stage and scanner are configured as shown in Figure 2.4. The sample holder is inserted face-down into a slot in the stage, spaced so that metal springs make electrical contact with the bars on either side of the sample. The clamping block is lowered or raised by means of an Allen-key screwdriver situated on top of this chamber (K) in order to provide thermal coupling between the sample holder and the flow cryostat (through the copper braid). This entire assembly in Fig. 2.4 is mounted on several springs for vibration isolation, and can be "floated" by unlatching and lowering a plunger at the bottom of the chamber.

To load a tip or sample into the chamber, the load-lock was sealed off at F and vented to ambient air through the turbo pump. The tip holder or sample holder, each made up of a "sandwich" of metal and/or ceramic with a grip loop at one edge, could then be inserted. A long rod with a pincer on the end extends the length of the load-lock; this pincer was closed on the tip or sample grip loop and the load-lock
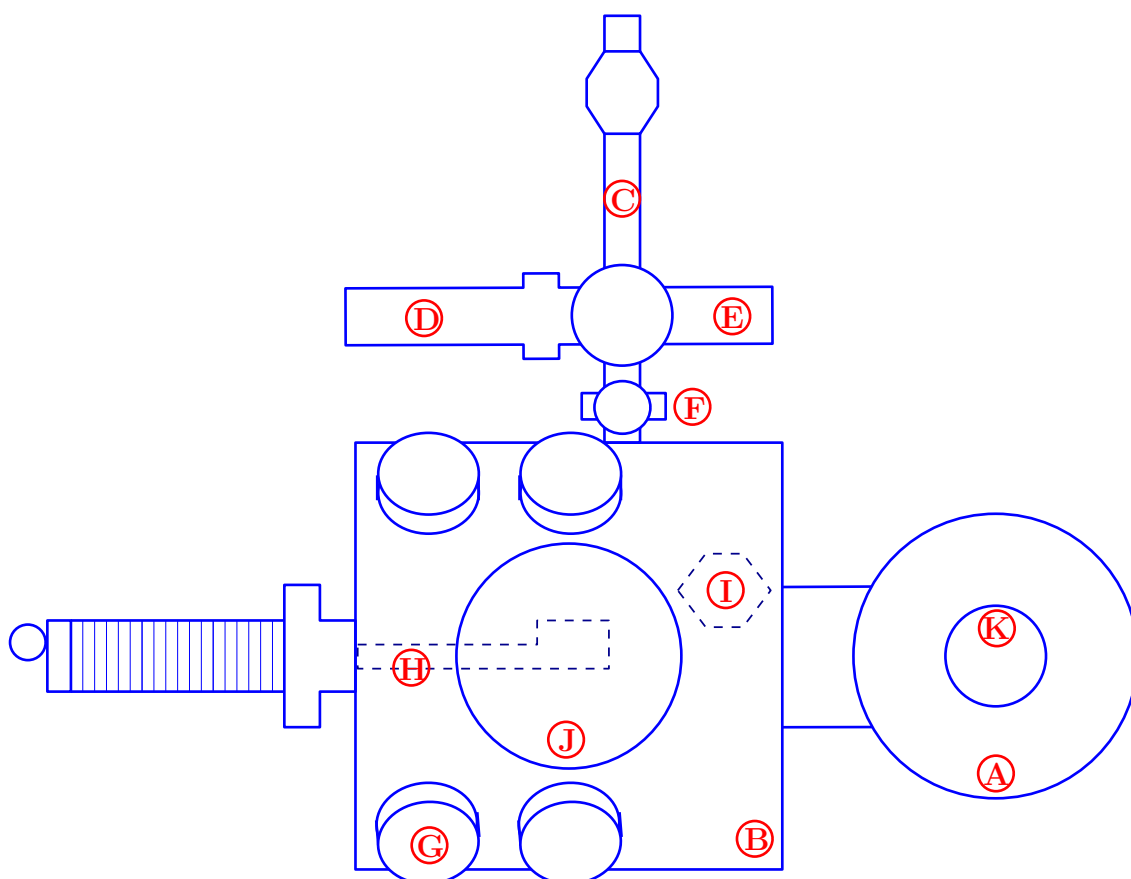
Figure 2.3: Schematic (top view) of UHV chamber housing Omicron VT-STM in U. of Maryland Surface Physics Group. See Section 2.3 for a full description of labels.
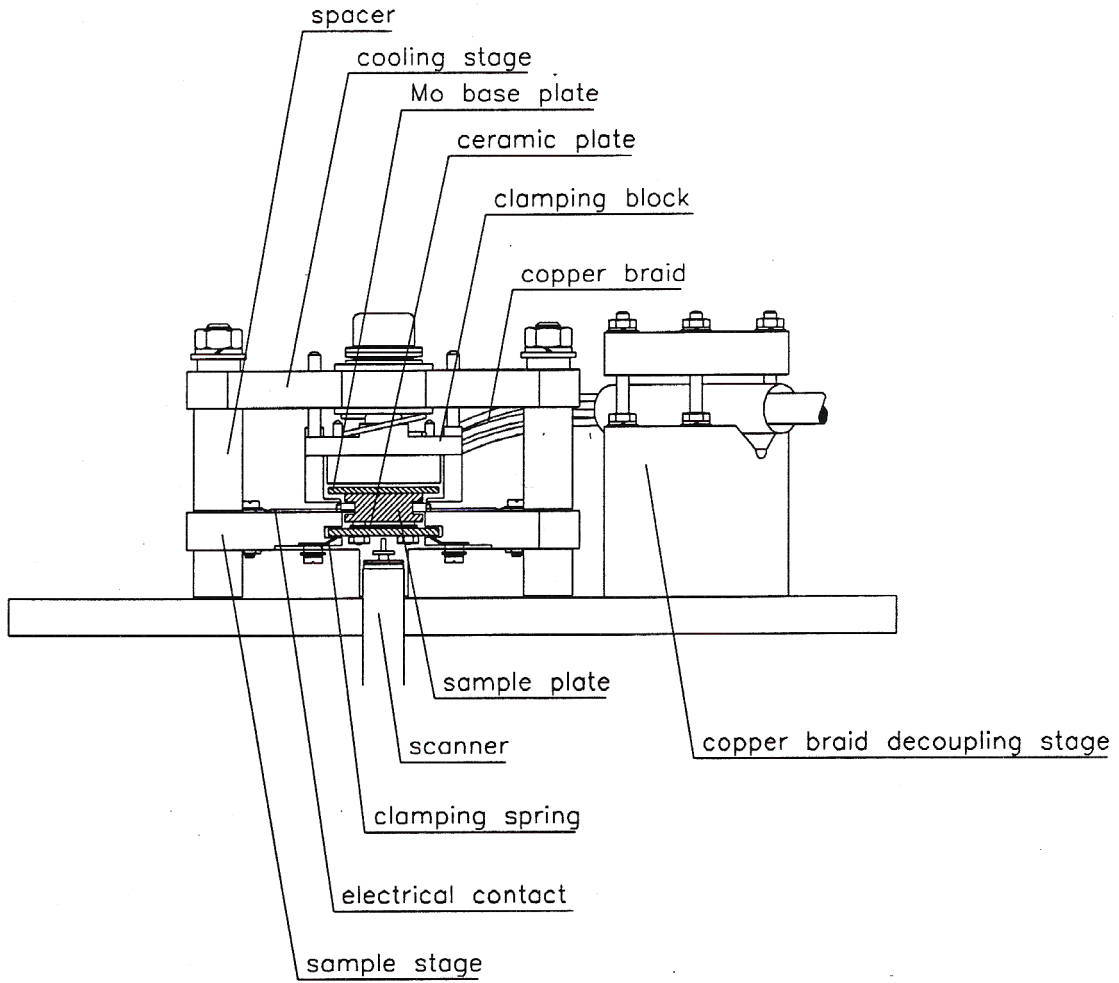
Figure 2.4: Omicron VT-STM sample mounting hardware configuration, respectfully borrowed from [60].

was pumped down for a minimum of 2 hours. Finally, valve F could be reopened and the load-lock pincer arm extended to transfer the tip or sample into the manipulator in chamber B, then into the carousel I or STM in A as needed.
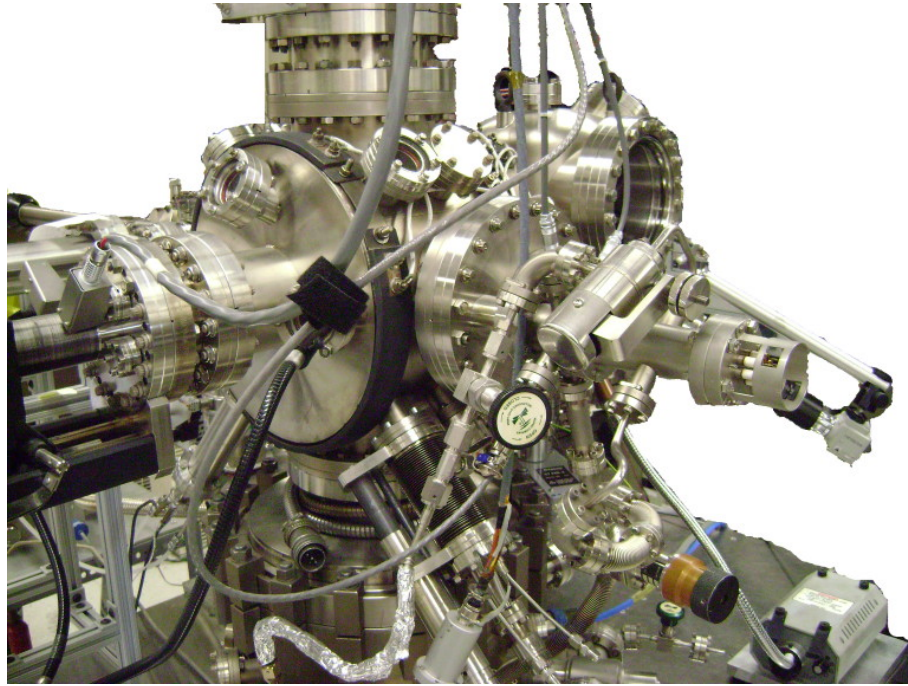
(a)
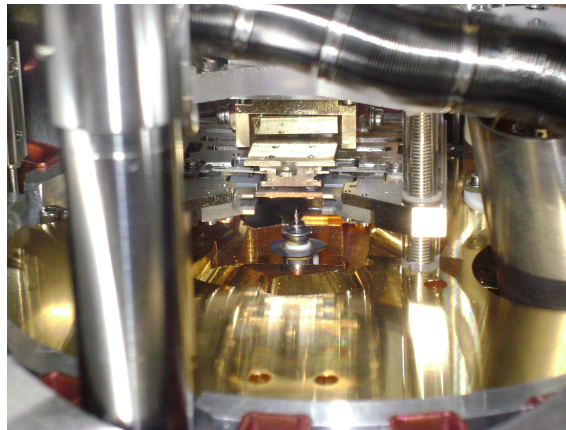
(b)

Figure 2.5: Photographs of the VT-STM system. (a) Wide view of the UHV chamber. The transfer chamber is in the center of the picture, with the STM chamber behind it to the right and the manipulator arm extending to the left. (b) Close-up view of the STM itself. The STM tip points upward and the sample is placed above it, as shown in Fig. 2.4. A vibration isolation spring is hidden inside the vertical tube on the left side of the image, and the wobble-stick bellows is visible along the top.

2.4 Tip preparation

STM probe tips are most commonly made from wire composed of tungsten (W) or of platinum/iridium alloy (Pt-Ir). Each material has its advantages and disadvantages in different environments [61]. Tungsten wires are stiff, which allows stable imaging; however, they are chemically reactive with certain elements, especially oxygen. On the other hand, Pt-Ir wires are softer (the addition of Ir to the alloy provides stiffening over pure Pt) but are chemically inert. This allows them to be successfully used in ambient and electrochemical STM. In this thesis, both kinds of tips were used to image different substrates under UHV conditions.

Experiments on silicon substrates were performed using W tips shaped by well-established procedures for chemical etching [62]. First, a 7 mm piece of 0.010" (0.25 mm) diameter wire was coarse polished in a 2.0 M KOH solution using a graphite rod as counter-electrode. A brief (< 1 sec) "flash dip" with 25 applied volts of alternating current was followed by a longer reaction of 50 seconds at 8-10 VAC. Fine adjustments to the tip shape were achieved through zone electropolishing with a bubble of 0.5 M KOH held around the tip inside a loop electrode of Pt-Ir wire, applying $\sim$5 VAC.

Pt-Ir tips were used to image organic molecules on graphite substrates. By holding a sharp pair of wire cutters at a shallow angle and cutting while pulling along the length of the wire, it is possible to create an atomically sharp point. Although it is located at a point on the wire's circumference rather than centered on its long axis as in the chemical etching case, it can be just as effective at obtaining high-

resolution images. This technique was applied to 0.010" diameter Pt-Ir wires to create tips in the lab. Commercial tips (NanoTips) created by a similar procedure were also employed.

All tips were loaded into and unloaded from the STM using tip holder assemblies of a size similar to that of the sample holders. A slot in the bottom plate, shaped like a skeleton keyhole, allows the round base of the tip to be inserted safely while preventing it from falling from the narrower part. A small magnetic disk at the base of the tip locks it in place, either at the narrow end of the tip holder slot or in a magnetic well on the scan head.

2.5 Sample preparation

Both silicon and graphite substrates were used in the experiments described in this thesis. Si(111) wafers (Virginia Semiconductor) with a miscut angle of 0.1° and resistivity 0.01-0.04 Ω·cm were cut using a diamond scribe into samples 1 cm long and 1 mm wide then mounted in Omicron sample holders. Highly-oriented pyrolytic graphite (SPI) was gently cleaved and cut to sample-holder size using a single-edge razorblade. Scotch tape was pressed onto one side of the graphite sample and rapidly peeled away to expose a clean surface.

2.5.1 UHV cleaning of bare Si(111) and HOPG

Cleaning silicon samples involves removing native oxide and surface species as well as forming the well-known (7×7) reconstruction on the (111) face [63]. After

attaching a power supply to sample contacts the Si substrate was resistively heated, initially to 600° C, as measured by an infrared pyrometer. Next, the applied current was rapidly increased until the sample temperature reached 1200° C and immediately decreased until the sample cooled to 875-900° C. Finally, the current was decreased slowly to take the temperature from ~850 to 700° ($< 10°$ per second), then returned to 600° C. This entire "flashing" procedure was typically repeated several times to ensure complete cleaning and full surface reconstruction. Figure 2.8a shows a square micron image of cleaned Si(111) with insets showing the (7×7) reconstruction at positive and negative bias.

Two possible errors are commonly encountered in this process: lingering too long at high temperatures, and moving too quickly through lower temperatures. The first error may be caused by stopping the fast cool-down prematurely, or by not having reached a peak temperature 1200° C. (However, it is also possible to melt and break the silicon sample by overshooting this mark.) An excess of time spent with the sample at these higher temperatures allows the formation of carbide crystallites [64], as shown in Figure 2.6a. The second error does not provide sufficent time for mobile Si atoms to reorganize into the less-dense (7×7) phase, and results in coexisting regions of reconstructed and unreconstructed silicon as shown in Figure 2.6b.

The process used for cleaning graphite substrates is substantially simpler than that for silicon. HOPG samples were mounted in Omicron sample holders that incorporated PBN heater plates. These were used to radiatively heat the graphite to 600° C or higher for a period of at least two hours. Following annealing, the
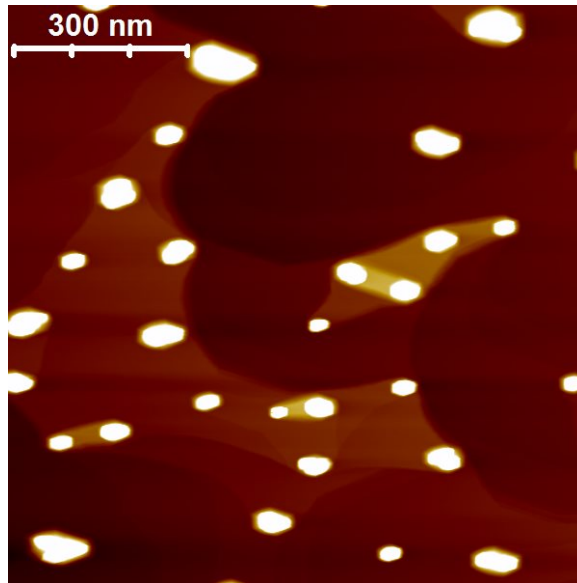
(a)
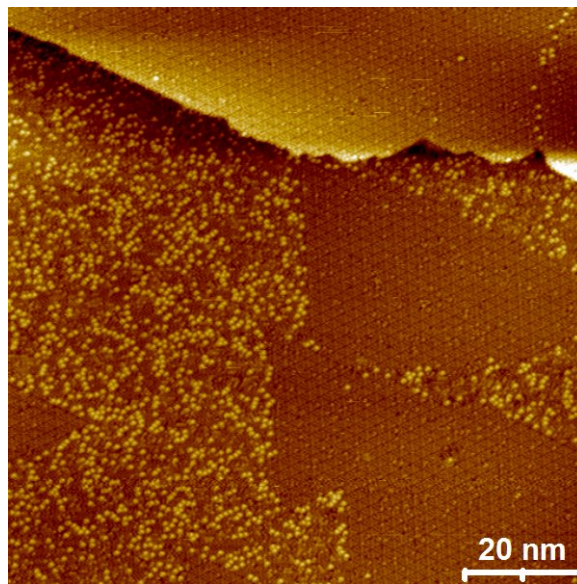
(b)

Figure 2.6: (a) Excessive annealing above 900° C results in carbon crystallite formation and step pinning. Height range: 19.77 nm. (b) Cooling too quickly prevents complete formation of the (7×7) reconstruction. Complete reconstruction is shown in Figure 2.8a.

(a)   (b)
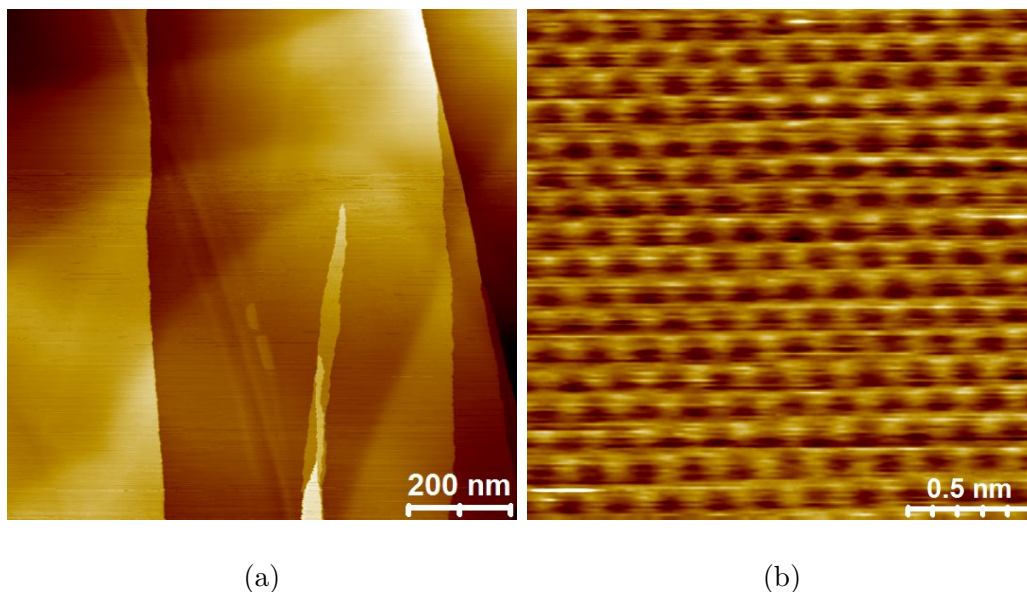
Figure 2.7: STM images of (a) HOPG terraces on a clean substrate, 1 μm^2 and (b) atomic resolution of clean HOPG, (2×2) nm^2.

power was turned down slowly enough to keep the sample holder assembly at a lower temperature than the sample itself, in order to avoid re-adsorption of evaporated molecules that may have condensed on the sample holder faceplate.

Atomic resolution images could be obtained on recently-cleaved graphite samples with no UHV cleaning, as shown in Figure 2.7. A triangular, rather than honeycomb, lattice is visible in STM of graphite due to the electronic effects of AB stacking [65]. In the event that residues built up on the HOPG surface that annealing could not remove, which happened gradually and only became an issue after several months of repeated deposition and annealing, the sample was removed from vacuum and re-cleaved with tape.

2.5.2 Ultra-thin oxide growth

Characteristics of, and preparation methods for, ultra-thin oxide (UTO) are of interest in order to better understand the progression of the oxidation process itself [66]. It is also important to catalog the functional properties and breakdown parameters of gate oxides used in state-of-the-art semiconductor device processes [67, 68]. Furthermore, for scanning tunneling microscopists, UTO is a convenient way to observe and conduct experiments on an oxide surface because they are thin enough ($<$ 5 oxide layers, on the order of 1 nm deep) to allow electrons to tunnel through to the semiconducting or conducting material beneath.

In the experiments described in Chapter 3, UTO samples of SiO_2 were prepared in a side chamber (load-lock labeled C in Fig. 2.3) with a base pressure of $< 10^{-9}$ Torr. A pre-cleaned Si(111) sample, confirmed by STM to have the 7×7 reconstruction, was moved into the side chamber and the turbo pump gate valve and valve F were both closed. Oxygen was added to the gas manifold until the manifold pressure reached 3.6×10^{-1} Torr. The valve connecting the gas manifold to the side chamber was slowly opened, then closed once the pressure reading was equilibrated. 25 seconds after the manifold pressure began to change, the turbo pump valve was reopened, once again pumping out the side chamber and removing the remaining O_2 gas. This exposure corresponds to $\sim 2.4 \times 10^6$ Langmuirs of O_2 [69].

Following oxygen exposure, the sample was outgassed in the main chamber at 573 K for 5 minutes to remove excess surface species. The resulting oxide surface was successfully imaged in STM with a tunneling current setpoint of 80-100 pA and

bias voltage of $\pm$ 2.5-3 V. UTO topography data is compared to that of bare Si(111)-7×7 in Figure 2.8. The oxide has a rougher appearance, and low-energy electron diffraction (LEED) measurements confirm no signature of the 7×7 structure. Note that bright spots in the UTO surface, normally interpreted in STM as corresponding to higher regions, are actually regions of thinner oxide [69]. Regions with higher conductivity will have greater apparent heights; thus, points at which there is more oxide that electrons must tunnel through will appear darker.

2.5.3 Physical vapor deposition of organic molecules

This thesis concerns studies of two adsorbed molecules: fullerene (C_{60}) and trimesic acid (TMA). Both types of films were prepared via physical vapor deposition inside the vacuum chamber immediately before imaging. C_{60} molecules were deposited from a Knudsen cell evaporator mounted on the transfer chamber after it was calibrated in the load lock using the crystal thickness monitor. TMA molecules were deposited in the load lock, with flux rates confirmed by the crystal monitor for each deposition.

The nucleation experiments described in Chapter 3 required extremely low coverages, so C_{60} was deposited slowly and the source was exposed to the sample for a short time. A 10 second exposure to sublimation at a source temperature of 385° C resulted in approximately 0.1 monolayer adsorbed on the UTO surface. While held in the manipulator, the Si/SiO_2 sample could also be heated resistively during deposition to explore film growth behavior at different surface temperatures.
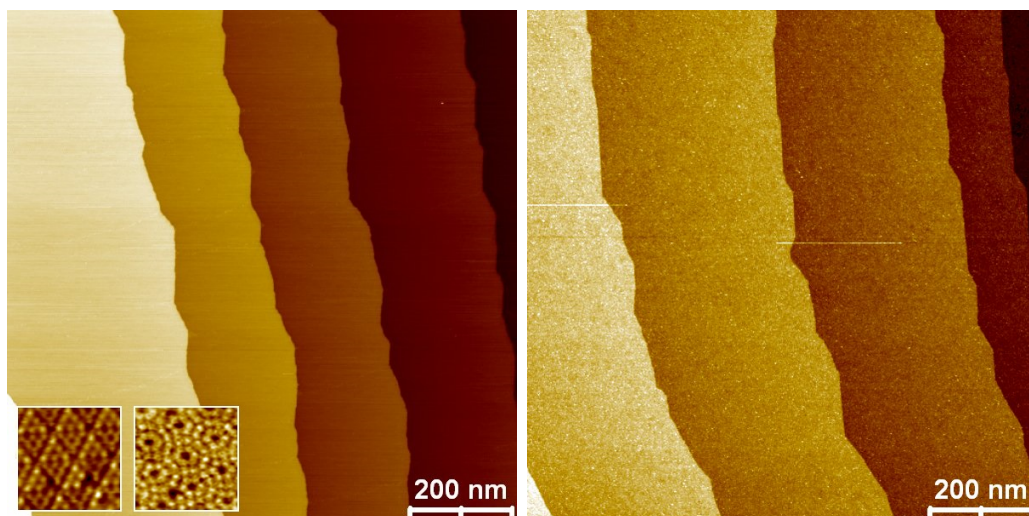
(a)   (b)
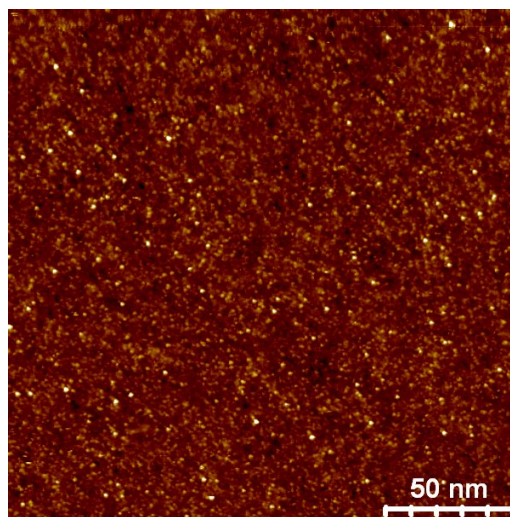
(c)

Figure 2.8: STM topography of Si(111) and UTO. (a) 1 μm^2 image of Si(111) surface after flashing. Insets show (7×7) atomic resolution at positive bias (left) and negative bias (right). (b) Si(111) covered with ultra-thin oxide. (c) Higher resolution image of UTO surface.
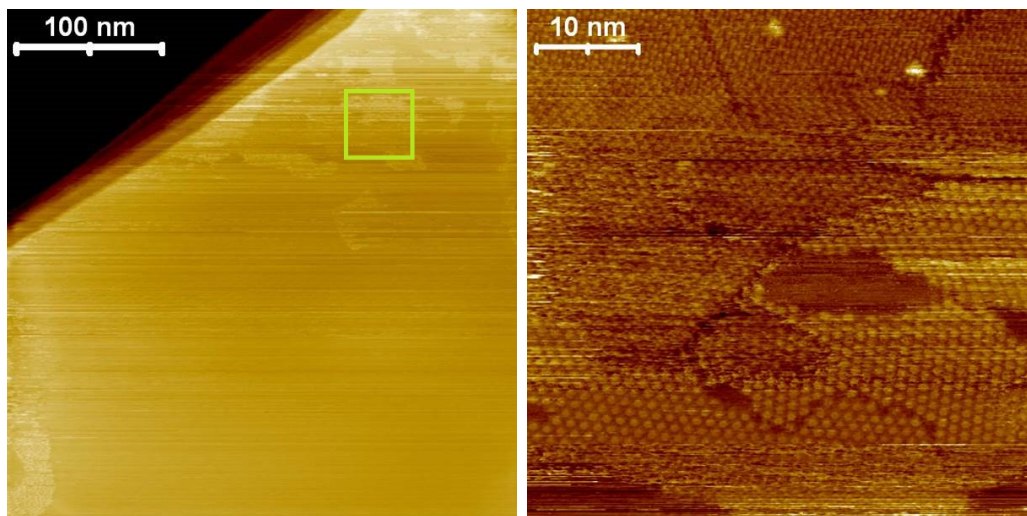
Figure 2.9: (a) 350×350 nm² STM image. Faint smudge-like regions can be seen in the upper right while the rest of the scan is smooth. (b) 50×50 nm² scan in the square marked in green. Several TMA grains are now visible.

The trimesic acid experiments, on the other hand, required substantially greater mass to be deposited, both because the formation of large-area ordered structures was desired and because organic molecules such as TMA on graphite have a sticking coefficient less than 1 (based on the difficulty of finding adsorbed molecules in STM, see Fig. 2.9). Therefore, TMA was sublimed at source temperatures of 210-235° C and exposed to the sample for 10 minutes or longer. Finding a reliable way to achieve the desired ordering in these films is an ongoing challenge which will be discussed further in Chapter 4.

Chapter 3

C_{60} on ultrathin SiO_2

The buckminsterfullerene (C_{60}) molecule consists of 60 carbon atoms arranged in a truncated icosahedron (Fig. 3.1). Its symmetry and uniform composition provide an elegant model system for studying the basic mechanisms underlying particle diffusion and island nucleation on a surface. While they have been observed to take specific orientations on surfaces at low temperatures [70, 71], at higher temperatures they are non-oriented and can be effectively modeled as hard spheres (*e.g.*, [72]).

C_{60} and its derivatives have also found many applications in the field of organic electronics. Pure C_{60} thin films have been used as the active semiconducting element in field effect transistors with modest and improving mobilities [73, 74, 75]. Organic photovoltaic devices often employ C_{60}, bare or functionalized, as an electron acceptor. Commonly studied donor/acceptor pairs, in which the HOMO and LUMO levels facilitate the flow of excited electrons, include polyphenylene vinylene (PPV)/C_{60} [76, 77], pentacene/C_{60} [78], and poly(3-hexylthiophene) (P3HT)/phenyl-C_{61}-butyric acid methyl ester (PCBM) [4]. Since thin film device characteristics are known to be strongly influenced by film morphology (see Section 1.1), careful investigations of C_{60} film growth are integral to the design of high-performance organic electronics.

The structural and electronic properties of C_{60} films have been studied in
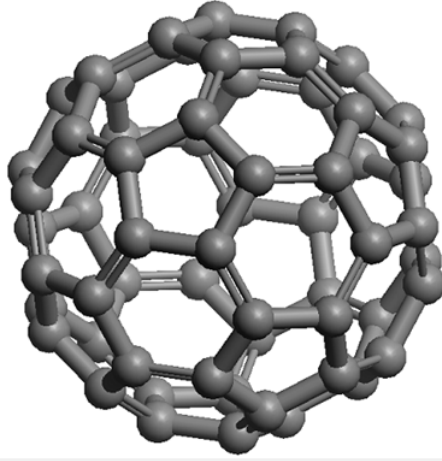
Figure 3.1: Ball-and-stick model of C_{60} molecule.

the context of single crystals [79, 80], bilayer structures [8], and neat devices [73, 74] typically hundreds of nanometers thick. However, the subtleties of the early nucleation stage have not been thoroughly examined. High-resolution imaging of C_{60} films on insulating oxide surfaces is required to model the growth kinetics of device-relevant films, but typical device oxide thickness of several hundred nanometers severely limits tunneling current and precludes the use of STM. By studying C_{60} film growth on an ultra-thin oxide approximately 1 nm thick, we retain chemical properties similar to those of the thicker oxides while allowing STM imaging of individual molecules.[1]

3.1   Experimental design

Ultrathin silicon oxide substrates were prepared using Si(111) wafers miscut $0.1°$ toward the [211] direction, according to the recipe described in Section 2.5.2.

[1]This chapter is adapted from Ref. [81], M. Groce *et al.*, Surf. Sci. 606 (2012) 53-56.

Following this, C_{60} molecules were deposited by thermal evaporation according to the procedures in Section 2.5.3. The temperature of the substrate was controlled during deposition and ranged from room temperature (298 K) to 483 K via resistive heating. After the film growth was completed, the sample was held at the given run's temperature for 60 seconds before it was allowed to cool in order for surface diffusion events to stabilize.

STM topography measurements were performed immediately, for 48 hours after film growth. Square topographs ranging in width from 80 to 100 nm (all at 512×512 px^2), in which an individual C_{60} molecule appears as a circle 7 to 10 pixels in diameter, were saved for further analysis. This amounted to approximately 1000 islands per substrate temperature. No meaningful change was observed in nucleation characteristics over the 48-hour time window, but accumulation of organic molecules on the STM tip and of vacuum residue species on the sample surface prevented additional high-resolution measurements.

After film measurement was completed, the C_{60} and oxide layers were removed from the Si(111) sample via the cleaning procedure described in 2.5.1. The same piece of silicon, or another piece cut from the same wafer, was used for the next film grown at a different temperature.

3.2   Capture zone scaling

A number of methods may be used in order to characterize the initial nucleation and growth of deposited films, most based around the concept of the critical

nucleus size i. The value of i reflects the number of particles in the largest *unstable* island. Thus, $i = 0$ corresponds to the case of stable monomers while $i = 1$ describes islands stabilized by dimer formation. Since critical nucleus size is related to grain size [12], analysis of i can provide a meaningful tuning parameter for thin film engineering as discussed in 1.1 as well as a precise physical description summarizing the delicate balance of forces governing the nucleation process.

One intuitive approach to determine i is to measure the areas of two-dimensional islands and compile the information into an island size distribution (ISD). There exists a significant relationship between i and the island size distribution [1, 82], but the precise nature of that relationship is still under investigation.

More recently the capture zone distribution (CZD) has been used in place of the ISD [83]. A capture zone is a Voronoi polygon constructed around the center of mass of an island, and represents the set of points closer to that island than to any other (*i.e.*, a proximity or generalized Wigner-Seitz cell). A particle that lands on the surface and diffuses in a random walk is most likely to end up attached to, or be "captured" by, the island in whose zone the particle landed. An illustration of islands and their corresponding capture zones is shown in Figure 3.3. The ISD and CZD generally give qualitatively similar single-peak distributions; however, the CZD always vanishes as the capture zone size goes to zero, while there may be a large number of small islands in the ISD.

A distribution commonly used to describe CZDs in two dimensions is the single-parameter gamma distribution (ΓD), which reflects the area distribution of

Voronoi cells constructed from points randomly placed in a plane [83, 84, 85]:

$$G_\alpha(s) = \frac{\alpha^\alpha}{\Gamma(\alpha)} s^{\alpha-1} \exp{-\alpha s} \qquad (3.1)$$

where s is the capture zone area divided by its mean and α is the "shape parameter" [86]. The gamma distribution has been invoked to characterize a diverse set of interesting systems [84, 87].

In 2007 the generalized Wigner distribution (GWD) [88, 89] was introduced as an alternative way to model the CZD, since it was shown to account for CZDs both from simulated and experimental data at least as well as the gamma distribution. The GWD has been successfully used to describe other spacing fluctuation phenomena in cases where there is a slight correlation between nucleation centers [90]; this is an advantage over the ΓD approach since island nucleation is not a completely random process. The GWD takes the form

$$P_\beta(s) = a_\beta s^\beta \exp{-b_\beta s^2} , \qquad (3.2)$$

where s is again the CZ area divided by the mean CZ area and β is the characteristic exponent. The terms a_β and b_β are β-dependent constants that enforce that $P_\beta(s)$ is normalized and has unit mean.

$$a_\beta = 2\Gamma\left(\frac{\beta+2}{2}\right)^{\beta+1} \Big/ \Gamma\left(\frac{\beta+1}{2}\right)^{\beta+2}$$

$$b_\beta = \left[\Gamma\left(\frac{\beta+2}{2}\right)\Big/\Gamma\left(\frac{\beta+1}{2}\right)\right]$$

Through a mean field argument, Ref. [88] proposed that s could be directly related to i; specifically it was argued that $\beta = i + 1$. Recent work indicates that one must go beyond mean field, which leads to the relation $\beta \approx i + 2$ [91, 92, 93, 94].
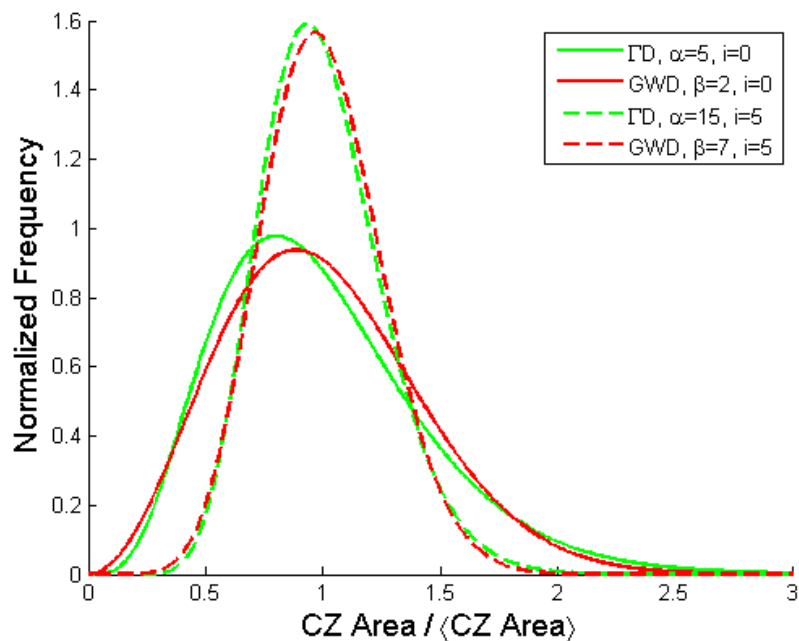
Figure 3.2: Comparison of ΓD and GWD for two values of i.

By virtue of the similarity of $P_{i+2}(s)$ and $G_{2i+5}(s)$ over the region near $1/2 < s < 2$ (where the statistics are best), the ΓD exponent α can be taken as a function of the critical nucleus size i, despite the lack of physical argument for this association. KMC studies of CZDs [92, 95] make use of the dimensionless parameter $\alpha \approx 2i + 5$. Figure 3.2 shows a comparison of GWD and ΓD curves at $i = 0$ and $i = 5$.

3.3 Data analysis and calculated results

Data were extracted from STM topographs using SPIP (Image Metrology). Raw images were corrected by a global plane fit and a line-wise histogram alignment, then processed using the Particle and Pore Analysis module set for a height threshold
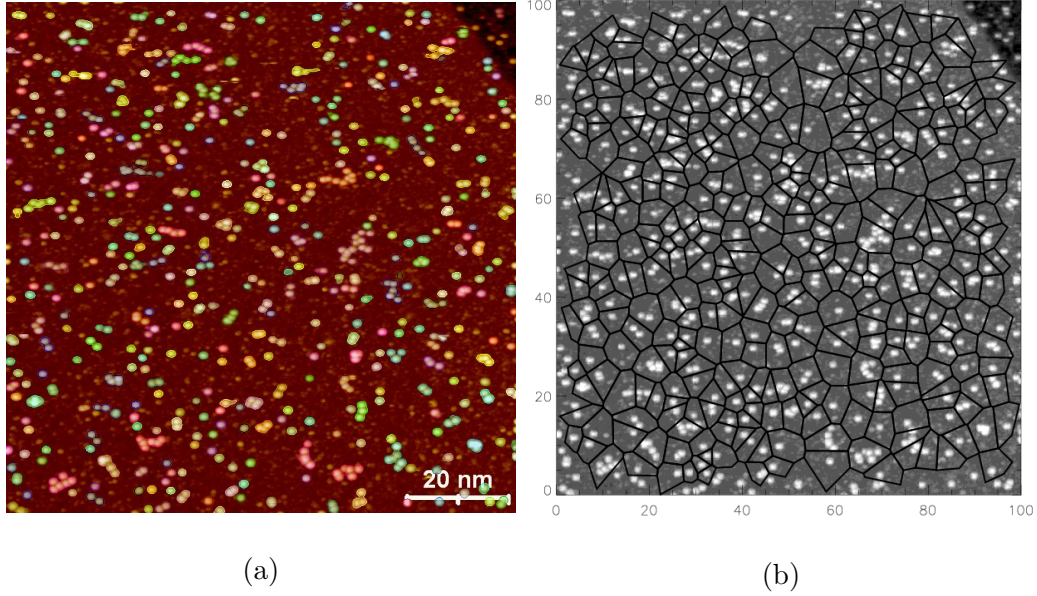
Figure 3.3: (a) Output of SPIP threshold analysis on a typical STM image, taken at 328 K. (b) Voronoi polygons as constructed in IDL for the same image.

of 60-80 pm and a minimum particle size of 0.9 nm in order to filter out false positives from oxide brightness variation. The exported (x,y)-coordinates of all island centers were then read into an IDL script to calculate the corresponding Voronoi cells and their areas. Figure 3.3a shows an example STM image after processing in SPIP, while Figure 3.3b shows the same image with capture zones as constructed in IDL.

At each growth temperature, the functional forms of the generalized Wigner distribution (Eq. 3.2) and the gamma distribution (Eq. 3.1) were fit by least-squares to histogrammed measurements of capture zone areas. Figure 3.4a shows an example histogram and corresponding ΓD and GWD fits. Extracted values of parameters α and β, and subsequently i, are listed in Table 3.1.

The plot of critical nucleus size i versus temperature in Figure 3.4b includes the
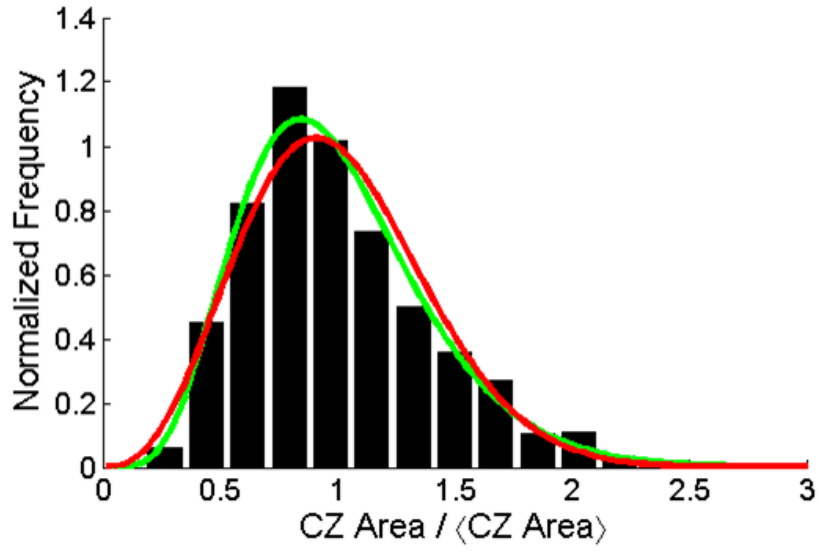
(a)
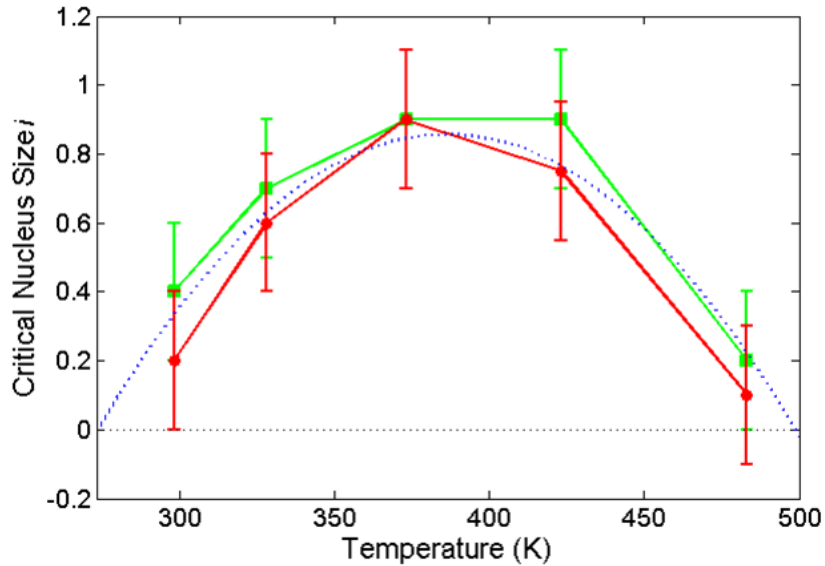
(b)

Figure 3.4: (a) An example capture zone distribution (CZD) histogram corresponding to islands grown at 328 K. The red curve shows the GWD fit ($i = 0.6 \pm 0.2$) and the green curve shows the ΓD fit ($i = 0.7 \pm 0.2$). (b) Temperature dependence of critical nucleus size i extracted from fitted values of GWD α (red circles) and ΓD β (green squares). The best fit parabola is shown as a dotted curve.

values from both the ΓD and GWD models. Error bars illustrate that the two models produced i values within one standard deviation of each other. Noninteger values of i reveal the heuristic nature of the critical nucleus size, but may be understood as a reflection of the detachment probability for a quasi-stable island of the next larger integer number of molecules [11]. Rather than a monotonic dependence of i on temperature, the trend seen in Fig. 3.4b shows a parabolic-shaped increase followed by a decrease. The peak of a least-squares-fitted parabola lies between 383-389 K with 95% confidence.

3.3.1   Capture zone sample size and statistical accuracy

The number of capture zones considered in analyses of this type are the primary factor in the uncertainty level of the critical nucleus size determination. Higher numbers reduce statistical noise and allow for more accurate fitting, which is why kinetic Monte Carlo simulations such as Refs. [83, 96] compute results for hundreds of thousands of islands or more.

Computation time and space can be limiting, but generally pose less of a hurdle

Table 3.1: Results of C_{60}/UTO CZD analysis, including ΓD and GWD fitting parameters, resulting critical nucleus size i, and island density N_{isl}.

Temperature (K)	ΓD α	ΓD i	GWD β	GWD i	N_{isl}
298	5.7 ± 0.4	0.4 ± 0.2	2.2 ± 0.2	0.2 ± 0.2	0.039
328	6.4 ± 0.3	0.7 ± 0.2	2.6 ± 0.2	0.6 ± 0.2	0.040
373	6.8 ± 0.4	0.9 ± 0.2	2.9 ± 0.2	0.9 ± 0.2	0.050
423	6.8 ± 0.3	0.9 ± 0.2	2.8 ± 0.2	0.8 ± 0.2	0.043
483	5.3 ± 0.3	0.2 ± 0.2	2.1 ± 0.2	0.1 ± 0.2	0.048

to KMC modeling than scan time, sample lifetime, and delicate tunneling conditions do to STM imaging. Multiple-tip effects, mid-scan tip changes, and human time constraints all contributed to the limited sample size (in the high hundreds for each temperature) in this experiment. However, it was still possible to fit the distribution functions to a reasonable x-axis binning of the data and obtain reduced χ^2 values of order unity.

It is worth noting that this is not always possible to achieve in island growth experiments. In unpublished collaboration with Prof. Michael Tringides of Iowa State University and Ames Laboratory, I applied the same capture zone analysis tools to his group's STM measurements of the system of Pb nucleation on Pb(111) islands on Si(111). Their publications [97, 98, 99] reported nucleation behavior that differs depending on whether the underlying Pb island has an odd or even number of layers. Ref. [98] deduced approximate values for i based on island densities in each case. It posed an interesting question about whether more precise values could be obtained through analyzing capture zone distributions, as well as whether the Pb/Pb(111)/Si(111) system could provide more experimental insight as to which model function (GD or ΓD) yields better fits.

Unfortunately, in that instance, the STM data did not provide sufficient statistics for the extraction of meaningful fitting parameters. Since a capture zone is defined by the distances from one island's center to those of its neighbors, islands at the edges of an scan image will necessarily not be assigned capture zones. Moreover, since the islands being considered in this system are themselves on another, larger island, the region of interest is limited further: even a comparatively broad scan

(a)

(b)
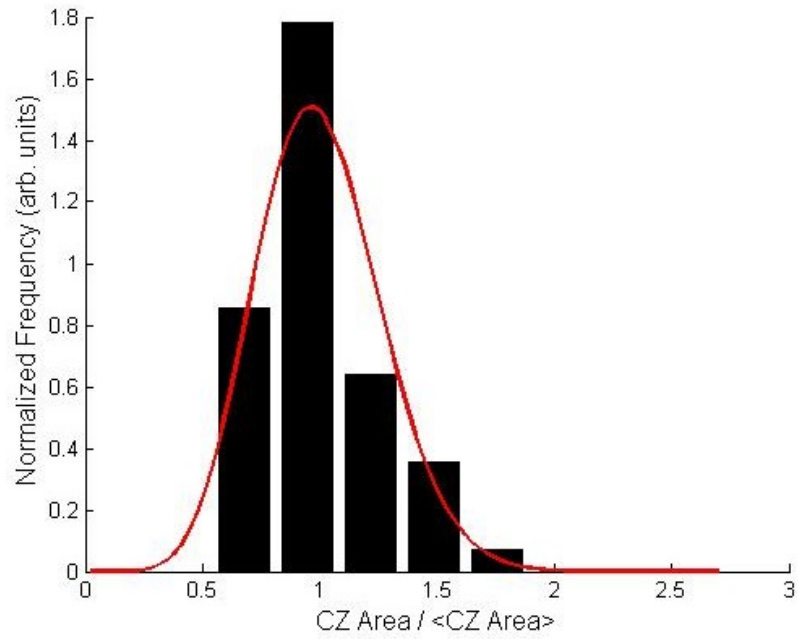
(c)

Figure 3.5: (a,b) STM images of Pb nucleation on Pb(111) islands on Si(111), provided by M. Tringides; (a), 107×122 nm^2, shows growth on a 4-layer Pb surface and (b), 403×162 nm^2, shows growth on 5 layers. (c) CZ histogram and GWD fit corresponding to capture zones calculated from (a). The GWD fitting parameter gives $\beta \approx 6$ ($i \approx 4$) but is based on fewer than 100 islands. A qualitative visual inspection of the histogram compared to the shape of the GWD shows poor correspondence.

area will not allow the inclusion of islands near the Pb/Si boundary. The Pb islands on Si are smaller than 100 nm in one or both directions and therefore can only hold a small number of Pb islands on top, as shown in Figure 3.5. This does mean that the system size is considerably smaller than the diffusion length, so island density saturates at a value independent of temperature and deposition flux rate [99]. It also means that CZD histograms like that in Fig. 3.5c cannot be well-matched to the models without much larger numbers of STM images than were available for my analysis.

More film nucleation imaging experiments would be a valuable addition to the development of capture zone distribution modeling. For useful results, though, high numbers of islands measured over large continuous regions are essential.

3.4   Discussion

An increasing value of i as temperature increases, as in the first portion of Figure 3.4b, may be understood in a homogeneous nucleation picture as being caused by increased surface diffusion with higher temperature, allowing for larger islands. However, it is unclear to what degree a homogeneous nucleation picture describes this system, and the decreasing portion of Fig. 3.4b still requires explanation.

For nucleated growth in pure systems, the island density N_{isl} is expected to decrease rapidly as temperature rises [100]. Values of N_{isl} observed in this system, listed in Table 3.1, show little systematic variation with increasing temperature (if anything, a slight increase). Such behavior could arise when defects or impurities

play a significant role. Given that the ultrathin oxide surface, as noted in Section 2.5.2, is not a flat facet but is instead rather irregular with local variations in oxide thickness, there is intrinsically a variation of binding sites such as might be produced by defects. (This complication did not hinder extraction of meaningful exponents from CZD analysis for pentacene on the same substrate with various dilute concentrations of pentacenequinone impurities [12].) It is possible that there are defect sites in the UTO which are activated or strengthened with increasing temperature, and that this activation counteracts otherwise homogeneous nucleation. Such a process may be compared to the growth of InAs quantum dots on GaAs(0001), in which nucleation has been described as a "sudden" or "explosive" process much faster than subsequent growth [101, 102]. This system shows spontaneous nucleation with $i = 0$ at surface steps and a morphological transition when those steps begin to erode [103, 104].

Further evidence in support of this defect-driven picture comes from the observation that the preponderance of islands, up to 75% at some temperatures, are monomers. In many analyses, monomers are excluded from the capture zone calculations since they are viewed as the fundamental mobile species. However, in the collected STM images monomers appear fixed in place on the substrate. Furthermore, if we were to exclude monomers from CZD analysis, the statistics are severely degraded so that many of the results become unreliable, but invariably the deduced value of β decreases by about 0.4 and the value of i is roughly zero. It is hard to rationalize this behavior in terms of a homogeneous nucleation picture, but it is consistent with defect-dominated growth as described above.

An increase in the fitting exponent (β or α) with temperature was also found for para-sexiphenyl islands on SiO_2, though likely for reasons [105] unrelated to defects or increased surface diffusion. Ref. [100] reported reentrant behavior reminiscent of the decrease in i observed here, in the case of epitaxial island growth as a function of what amounts to increasing temperature; however, their observations seem more appropriate to larger values of i than in our case, so that edge diffusion on larger islands plays a role. Adding to the complication is the fact that codeposited impurities can increase *or* decrease the critical nucleus size, depending on the physical role they play [106, 95].

Further study of the C_{60}/UTO system is necessary in order to develop a clearer physical picture of the initial nucleation process. Nevertheless, the unusual temperature-dependence of i observed here can be applied to organic device preparation techniques and underscores the usefulness of capture zone analysis to characterize thin film nucleation and growth.

Chapter 4

Structural phases of TMA on HOPG(0001)

Investigation of the self-assembly and ordering of trimesic acid molecules on graphite was motivated by the desire to modify the electronic structure of graphene with a periodic interaction distinguishing its two degenerate sublattices, as discussed in Section 1.2. Hydrogen bonding facilitates the creation of a stable molecular superlattice physisorbed on graphene, which has the potential to open a band gap.

Rather than begin exploring this system on graphene samples, which are cumbersome to fabricate and difficult to locate for imaging in an STM-only system, I used substrates of highly-oriented pyrolitic graphite. The basal plane of graphite is identical to graphene in structure. Experiments concerned with the assembly of molecules into physisorbed networks are most sensitive to the top layer of substrate atoms and are therefore unlikely to be drastically different on graphene versus graphite. (Following the same argument in the opposite direction, graphene has been used as a model substrate in DFT simulations of adsorption on graphite [51], corroborating the intuition behind this approach.)

Trimesic acid was deposited via physical vapor deposition on clean HOPG substrates according to procedures described in Sections 2.5.1 and 2.5.3. Samples were then imaged with STM in UHV at room temperature, which is to our knowledge the first instance of successful imaging of TMA on graphite under these conditions.
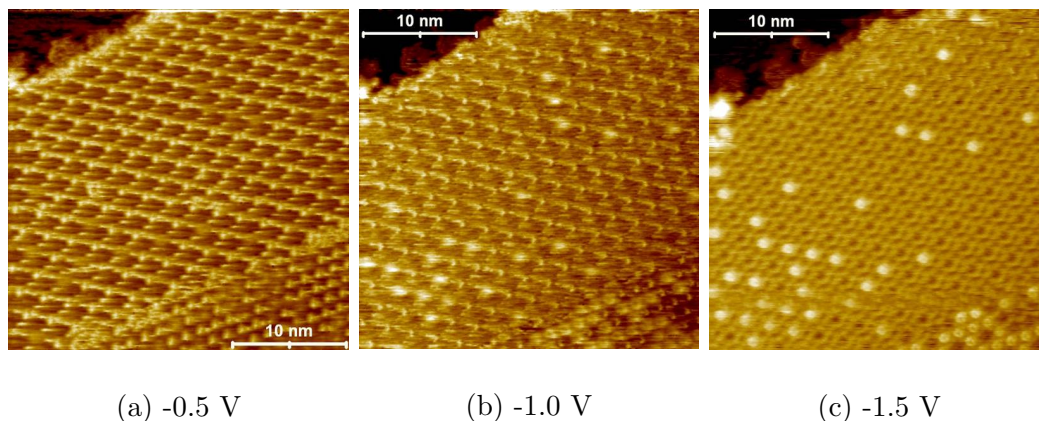
(a) -0.5 V   (b) -1.0 V   (c) -1.5 V

Figure 4.1: One region of a TMA network on graphite, beginning at a step edge and extending across the terrace. The images were acquired at 100 pA and (a) -0.5 V, (b) -1.0 V, and (c) -1.5 V. At -0.5 V the TMA lattice is not clear and could be confused with Moiré patterns in HOPG. At -1.5 V, molecular resolution is achieved.

Much previous work considered lattice formation at the liquid-solid interface, performing STM inside a droplet of heptanoic acid and other solvents with dissolved TMA [46, 47, 49]. UHV studies have previously been restricted to low-temperature, based on the understanding [43] that "STM images could not be taken at room temperature due to the weak binding of the molecules to the substrate." Film instability was an issue in the present investigation, but overcoming other challenges such as the low sticking coefficient of graphite (see Section 2.5.3) and finding appropriate tunneling parameters did allow molecular-resolution imaging to be achieved. Figure 4.1 shows the strong voltage-dependence of the appearance of TMA in STM images. Unless otherwise noted, all topographic data of this system were acquired at a current setpoint of 100 pA and a sample bias of -1.5 V relative to the tip; a bias magnitude of 1.5 V was the minimum required to image TMA.

4.1 Porous hexagonal networks

The predominant phases observed in these experiments were H_1 and H_2, consistent with other studies of TMA on graphite [49, 45, 50]. STM confirms the identification of H_1 with a primitive lattice vector of 1.7 nm (7 times that of graphite in-plane) and H_2 with a primitive vector of 2.7 nm (11 times that of graphite). Since the HOPG surface was best imaged at $|V|$ of 500 mV or below and the TMA lattice did not become clear until $|V|$=1.5 V, it was not possible to resolve both in the same STM scan. Attempts to image one immediately after the other consistently resulted in blurry images due to poor tip condition, probably due to molecules suddenly drawn to or kicked off the tip. Therefore, regrettably, the exact alignment cannot be determined from these data but may be obtainable in future STM studies.

Bright spots inside the pores in these images are extra TMA molecules [47, 43] referred to as "guests." Other molecular species, while possible in TMA host systems [52, 107, 108], can be ruled out since the experiments were performed in UHV conditions and only exposed to a TMA source. Lack of resolution inside the pore is consistent with earlier works (*e.g.*, Figs. 5 and 7 in [43]) and can be attributed to the availability of multiple positions within a pore for a guest molecule to attach. Guest molecules are mobile and likely switch between positions rapidly even when stable within a single pore. Host/guest structures will be described in more detail in the following section.

Other structures H_n for $n > 2$ were also rarely observed. Approximately one in 20 film preparations yielded images of higher-n networks, which contained
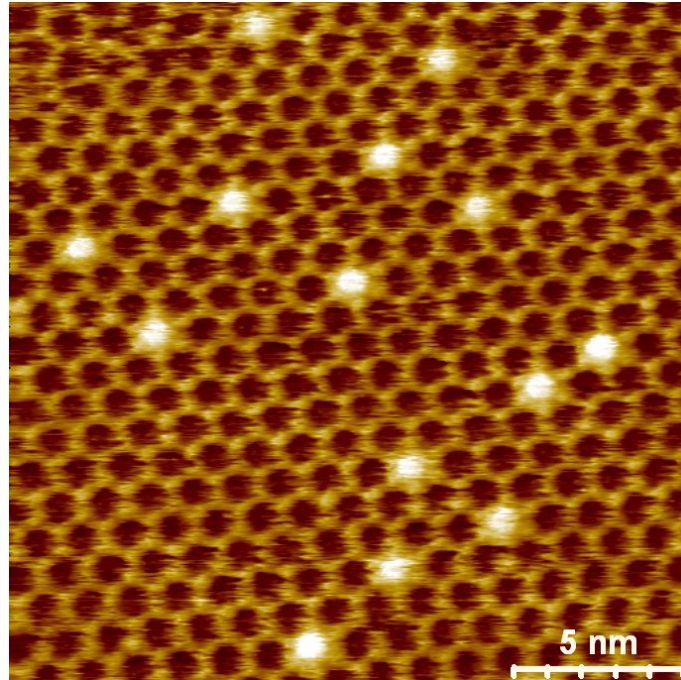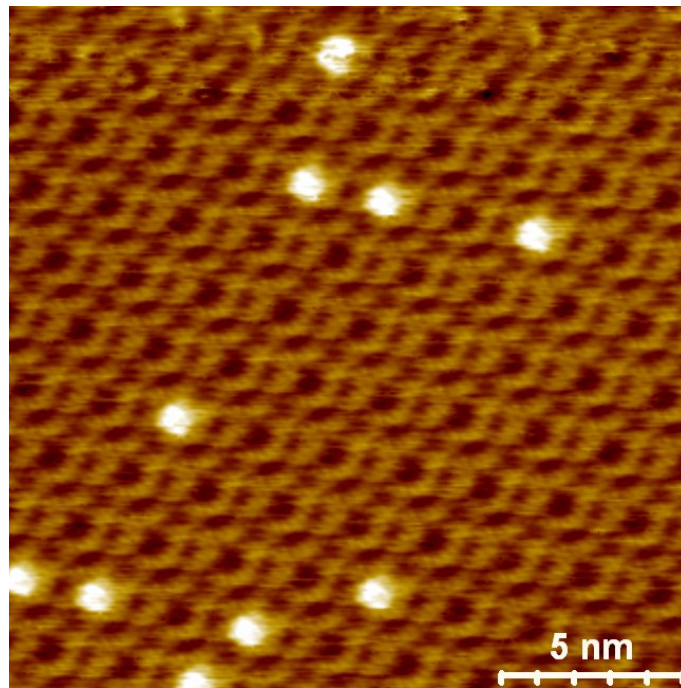
Figure 4.2: (a) Honeycomb phase H_1 and (b) Flower phase H_2 of TMA on graphite.
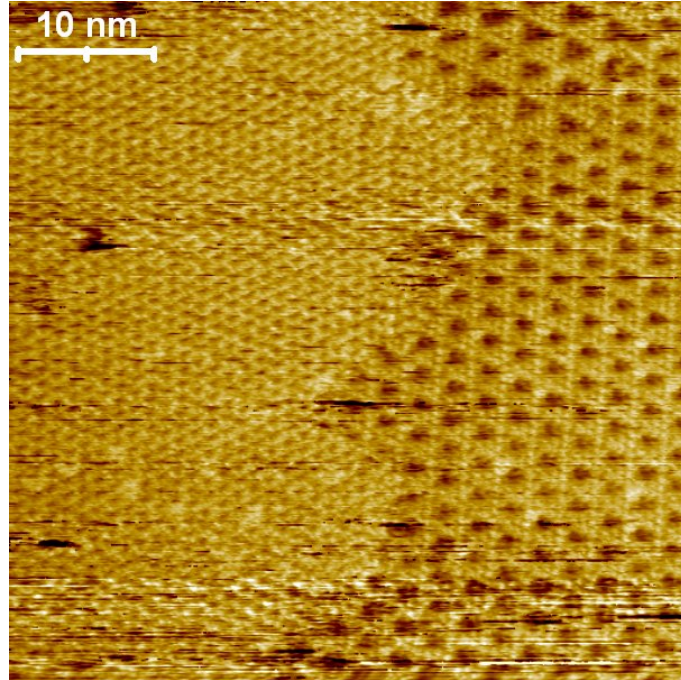
(a)
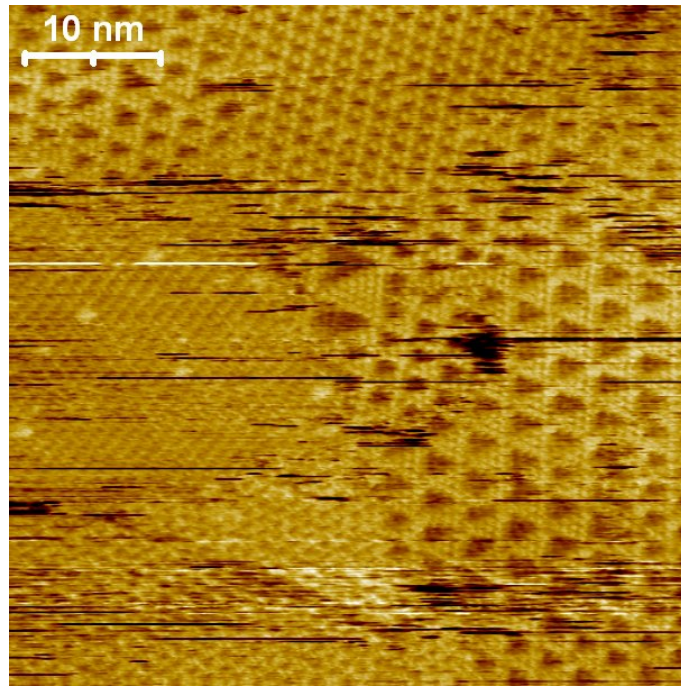
(b)

Figure 4.3: H_n TMA networks for $n > 2$. (a) H_2 on the left with H_3 and H_4 on the right. (b) H_1 up to H_7 coexist in this region.
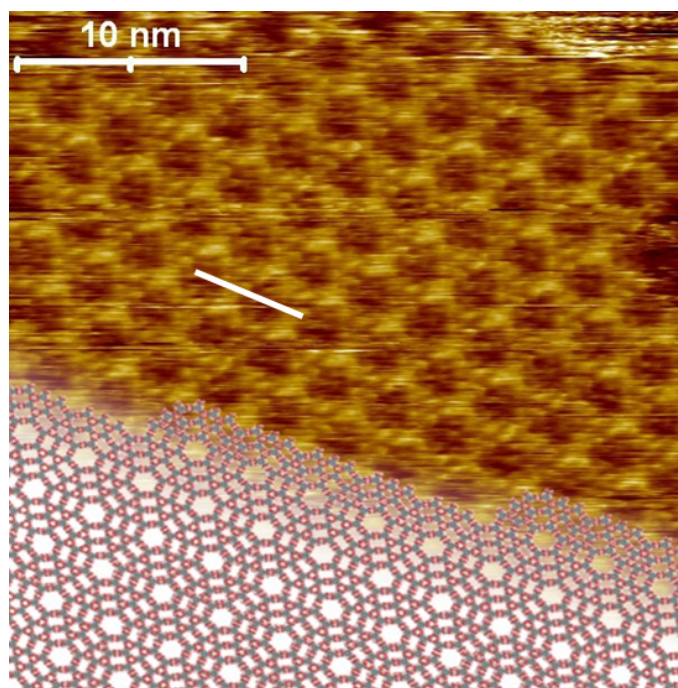
(a)
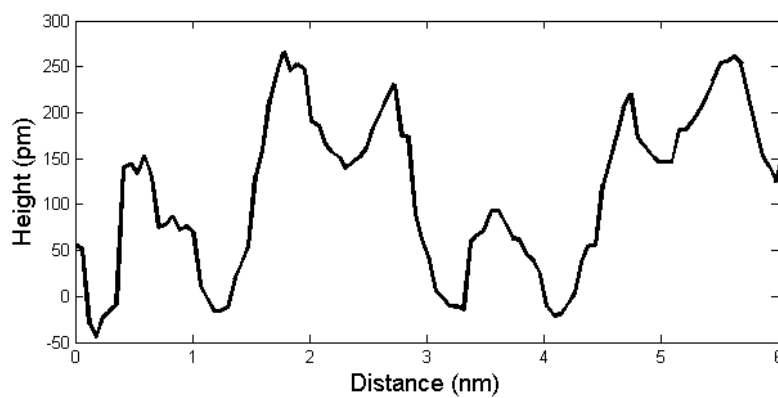
(b)

Figure 4.4: (a) Molecular-resolution STM image of H_3 with structural illustration superimposed. The STM topography appears to show all pores as filled, though for clarity this is not included in the illustration. The white line indicates the location of (b) a line profile cutting across four triangles at mid-height, showing the alternating bright and dark regions.

regions corresponding to many different values of n in a 50×50 nm^2 scan as shown in Figure 4.3. A feature of higher-n networks that was not observed for H_1 or H_2 is the alternation of bright and dark regions in the lattice. One triangle of molecules $(1+\cdots+n)$ per unit cell appears taller than the other, as can be seen in molecular-resolution STM of H_3 (Fig. 4.4). This may be caused by inequivalent alignment with the underlying graphite, although it is not clear why this would be such a strong effect in $H_{n>2}$ while never apparent in the honeycomb or flower phases. It is possible that the energetically favorable alignment for H_1 and H_2 is non-symmetry-breaking, but is symmetry-breaking for $n > 2$; further calculation and experimentation are needed to confirm this.

4.2   Host/guest structures

Guest molecules were always present, in varying concentrations, in the TMA lattices imaged in this work. A great deal of research has been done on the formation and dynamics of host/guest systems [109, 110] such as these. While this is not directly relevant to the problem of using molecular adsorbates for graphene symmetry-breaking, it deserves consideration to the extent that guest molecules present in porous hexagonal networks could impact the film's electronic structure. It may be necessary to grow films without guests, or with as few as possible, in which case a better understanding of what causes pore filling could prove useful.

Following one instance of mild annealing at $\sim$130° C for 10 minutes, long-range ordering (at least 500 nm wide) of TMA molecules was observed. In addition

to increased stability of the hexagonal network, which persisted for many hours, the host sites in the film were completely filled. Both honeycomb and flower phases were imaged (see Figure 4.5) but higher-n H_n were not, consistent with the as-grown films. However, in these images, the brightest spots in the lattices were consistently *not* near the central TMA ring and spreading over the whole molecule as before, but instead located at the hydrogen bonds connecting adjacent molecules. This suggests a switch from LUMO to HOMO imaging, based on the calculations of Ref. [51].

Unfortunately, this type of structure could not be recreated for further study in subsequent deposition/annealing attempts. Idiosyncracies of the sample holder configuration may be responsible; it is possible the first film ordering was created by TMA molecules desorbing from the graphite and collecting on the sample holder faceplate, then condensing again onto a nearby patch of the graphite surface as it was cooled. The images in Figure 4.5 were obtained while scanning near the edge of the faceplate window, and may be the result of an extremely fortuitous choice of approach site.

Prolonged scanning of as-grown films revealed a gradual but consistent increase in guest molecule concentration over time. Table 4.1 summarizes five series of STM images acquired with as fast a scan speed as possible without blurring. At different locations on the same film, all show a rate of increase of $\sim 5 \times 10^{-5}$ guests per square nanometer per second. In more intuitive terms, this corresponds to approximately one additional host site receiving a guest in a 50×50 nm^2 area every eight seconds.

What causes this influx of guest molecules? No additional material is being deposited on the surface during scanning. One possibility is that tunneling through
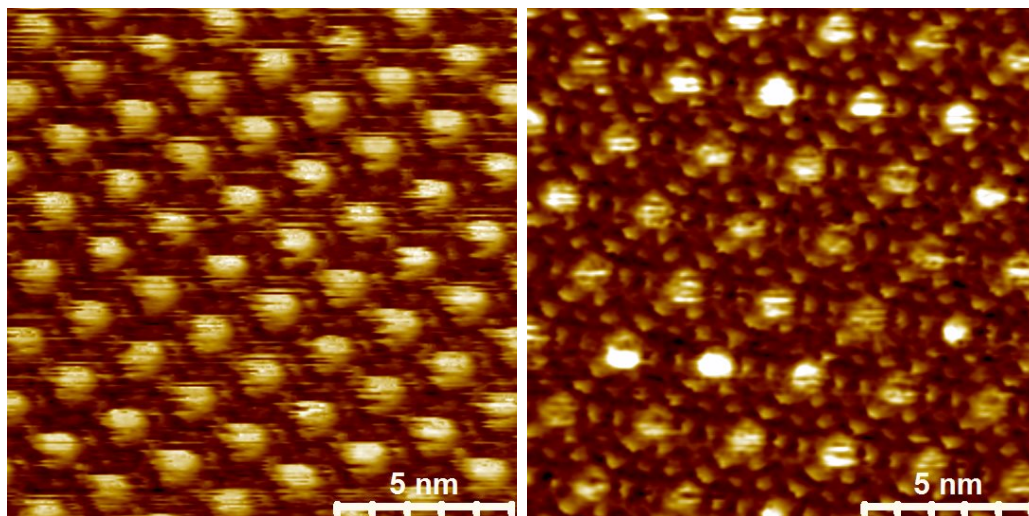
(a)

(b)
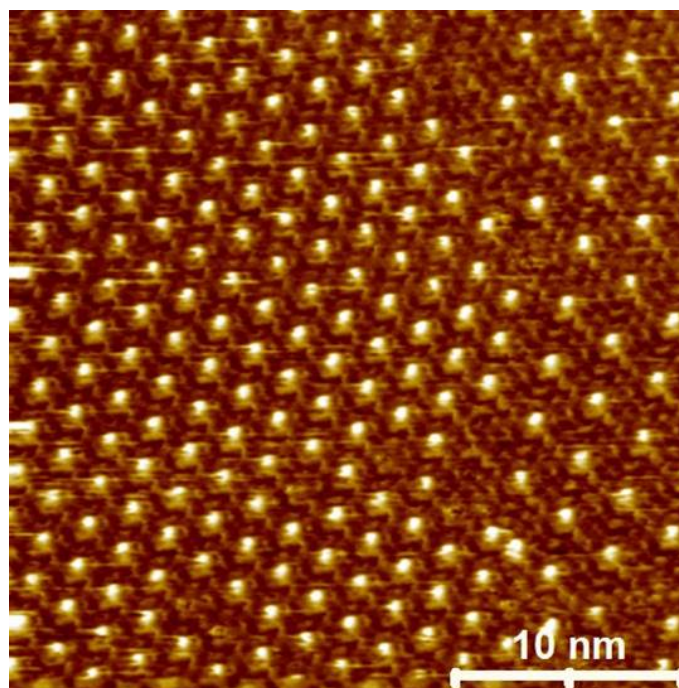
(c)

Figure 4.5: (a) Honeycomb phase H_1, (b) flower phase H_2, and (c) a region around an H_1-H_2 grain boundary observed in the annealed TMA film discussed in Section 4.2. Carboxyl groups involved in hydrogen bonds are brightest in the lattice, corresponding to the adsorbed molecular HOMO calculated in Ref. [51]. Almost every pore is filled with guest TMA molecules.

Table 4.1: Fast STM scans show guest molecules hopping from pore to pore, but also show a consistent increase in the total number of guest molecules present. Here the results of these "movies" are summarized by their scan area, total number of scans, time per scan and total time for all scans, initial and final numbers of guest molecules observed, and overall rate of guest increase.

Area (nm^2)	Scans	t_{scan} (s)	t_{TOT}	Initial #	Final #	Rate (#/nm^{2}s)
15×15	26	43.7	18:56	20	36	6.3×10^{-5}
15×15	14	87.2	20:21	30	47	6.2×10^{-5}
20×20	21	87.2	30:31	67	95	3.8×10^{-5}
20×20	21	130.7	45:45	128	215	7.9×10^{-5}
30×30	13	174.2	37:45	60	119	2.9×10^{-5}

the STM tip draws TMA to the current scan area. This is suggested by molecular manipulation studies such as [52]. However, one cannot yet rule out the explanation that TMA molecules are simply diffusing around on the graphite surface, tending toward a more stable film configuration in which all pores are eventually filled.

4.3 Film dynamics

Perhaps the reason Griessl *et al.* in Ref. [43] claimed that TMA networks could not be imaged at room temperature is the fact that most of the HOPG surface appears to be covered with a 2D gas of molecules. Ordered regions emerge out of the gas and can disappear back into it. Density waves (Fig. 4.6), the accumulation of gas-phase molecules into a series of evenly-spaced "rings" separated by less-dense regions, are sometimes visible around the edges of molecular lattices. These waves may be a signature of Friedel-like electronic oscillations attracting TMA molecules to charged areas.
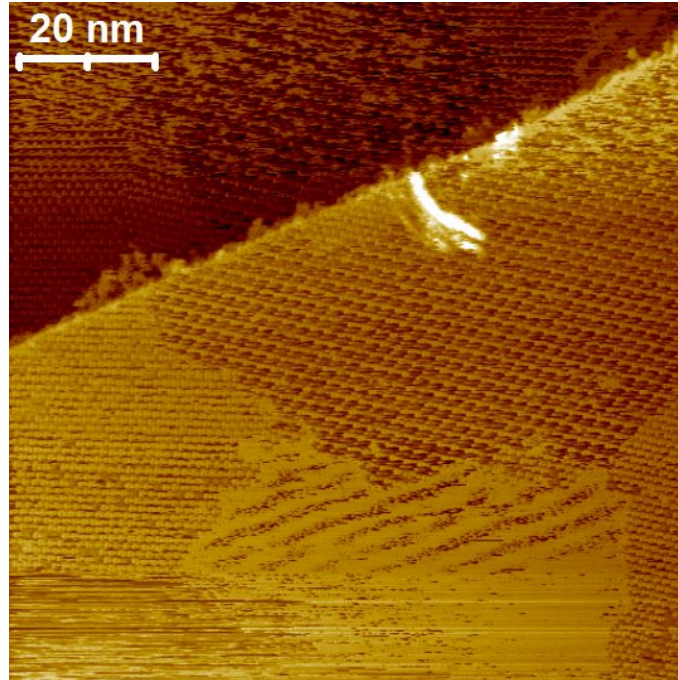
(a)
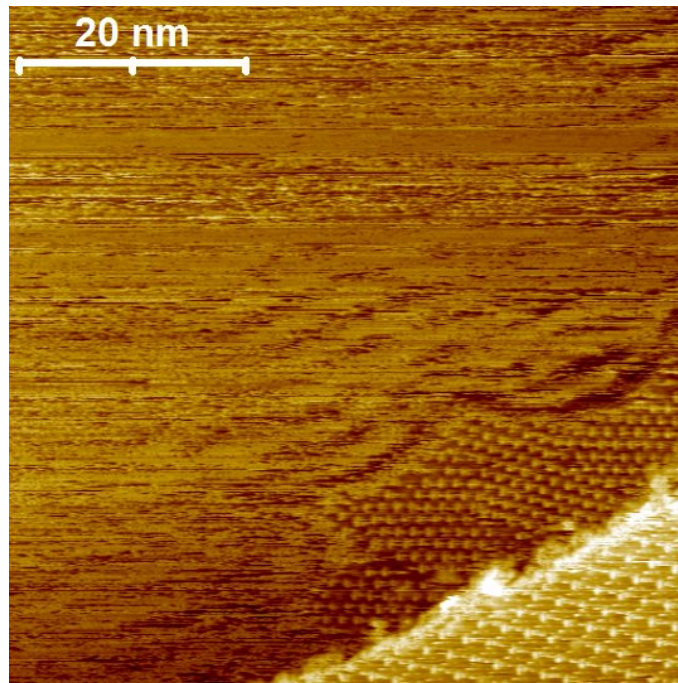
(b)

Figure 4.6: Two examples of density waves observed in the 2D gas of TMA pervading the graphite surface. Both images were taken at -500 mV. $\lambda = 3 - 3.5$ nm.

As discussed in Section 4.1, distinct phases of TMA (typically H_1 and H_2) often coexist in the same ordered structure. Grain boundaries can be seen between different orientations of the same phase or between different phases. The boundaries move as TMA molecules reorder themselves from one grain to another. Figure 4.7 shows two images, taken six minutes apart. The edge of the flower region, in the first scan concave and jagged, advances down and right by the time of the second scan where it appears as a straight line. An oblong area approximately 5×10 nm^2 in the top half of the image is ordered in the first scan but appears smooth (in gas phase) in the second, providing additional available molecules to construct the expanded area of denser H_2 lattice. The increase in host pore occupancy discussed in the previous section may be caused, at least in part, by reordering molecules leaving a denser phase and having no nearby space to fill in the adjacent less-dense grain.

Guest molecules can also be seen to have hopped from one pore to another. Many hopping events may have happened in the time it takes for one STM scan to complete, so it is difficult to quantify any aspect of the process. The data in this experiment may have, like a strobe light in a dark dance hall, only captured a hint of the complexity of the molecules' motion. Nevertheless, the images in Figure 4.8 strongly suggest the guest molecule movements indicated by the green arrows.

4.4   Discussion

TMA has been shown to create porous hexagonal networks H_n for $n = 1, 2$, and greater values on the graphite surface after physical vapor deposition. The fact
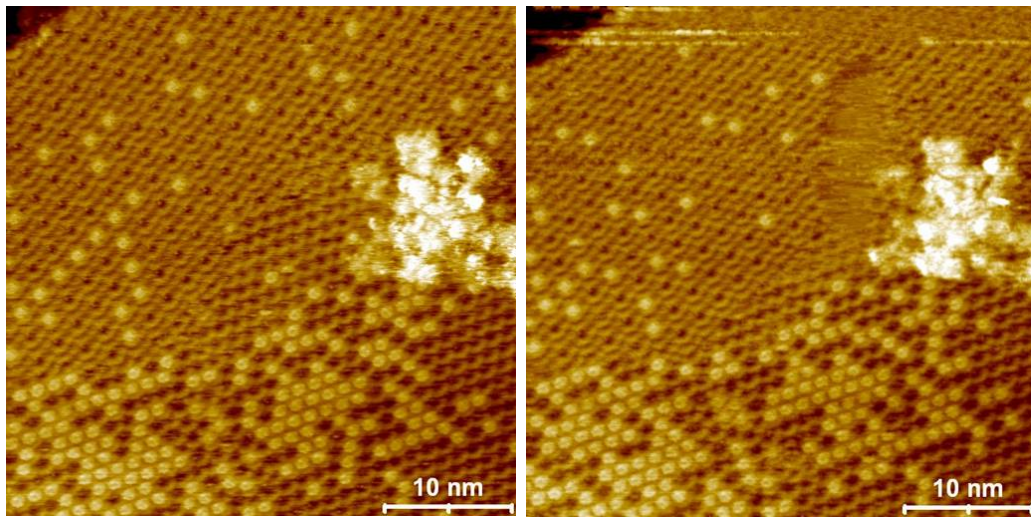
Figure 4.7: Two consecutive STM images of a grain boundary between H_2 (upper left) and H_1 (lower right). (a) The boundary, crossing near the center of the image, is jagged. A protruding area of H_1 is surrounded by H_2. (b) Six minutes later, the H_2 boundary has straightened and pushed forward into the region formerly occupied by H_1, while an oblong portion of the top half of the image has reverted to a 2D gas phase.
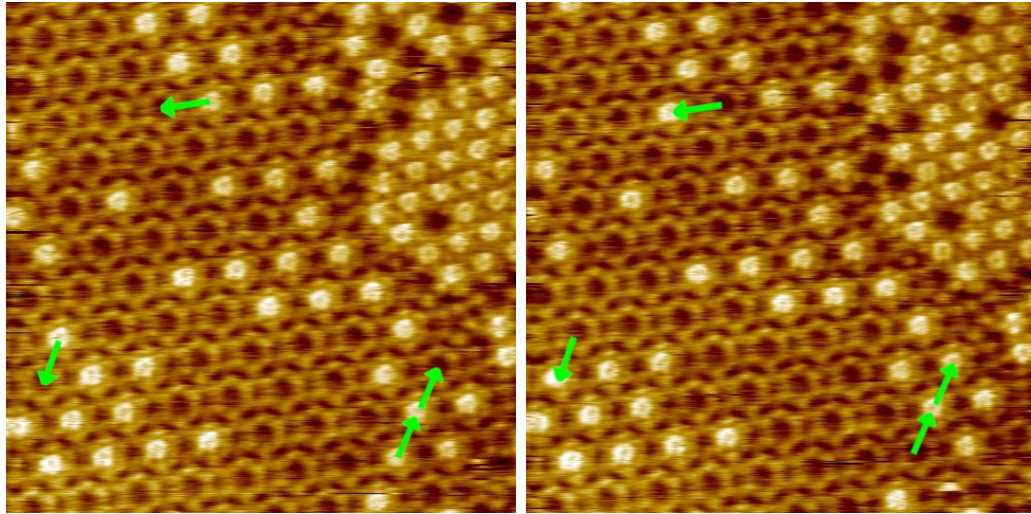
Figure 4.8: Guest molecule hopping. 20×20 nm^2 STM images (a) and (b) were taken 87.2 seconds apart. Probable movements for four guest molecules are indicated by green arrows.

that these networks are observable at room temperature is a promising sign, but further work must be done to increase the networks' stability over time before this system can be considered for device applications.

Annealing may prove to be a useful tool in this endeavor. Care must be taken to keep temperatures relatively low, since ordered molecules are already prone to diffuse away from the lattice or desorb spontaneously. However, these experiments suggest that pore-filling with guest molecules is related to increased film stability. The symmetry-breaking implications of guest TMA molecules is difficult to ascertain; perhaps TMA networks should be filled with another, slightly larger, molecule that is more stable within a pore in order to create a system that is both stable over longer timescales and a more certain symmetry-breaker.

Another option, not explored in this thesis, would take inspiration from the solid-liquid interface studies. Long-range ordered networks of a single phase can be created by appropriate choice of solvent [46]. An ideal lattice could be created if the excess solvent can be removed without more TMA precipitating from it. Of course, it also remains to be seen if this lattice would remain stable as it appears to be in liquid, or if it would take on the properties of a PVD-grown film once the liquid was removed.

Chapter 5

Probing local density of states in TMA/HOPG(0001)

Measuring the electronic density of states in trimesic acid films is crucial to determining the effects of these molecular networks on graphene band structure. Since others have studied TMA primarily in the context of host/guest architectures, no previous work has investigated the DOS in TMA on HOPG or on graphene. In conjunction with theoretical research also being conducted in the UMD Surface Physics Group [111], I have performed the first scanning tunneling microscopy measurements of TMA on graphite in order to explore this system.

Future use of TMA films in graphene band structure engineering will require further investigation of TMA/graphene electronic properties, through STS, transport measurements, or other techniques that provide insight into the DOS. Experiments on graphite cannot tell the whole story because, although the crystal structures of HOPG and graphene surfaces are identical, their band structures are not. Nevertheless, by comparing STS spectra on pristine graphite to those taken from TMA films on HOPG, one can begin to understand how the presence of TMA lattices can affect the electronic properties of graphitic materials.

Tunneling spectra were acquired in room-temperature UHV conditions alongside the STM topography data described in Chapter 4. A 48×48 grid was overlaid on a scan frame of interest, and individual spectra were saved from each point in
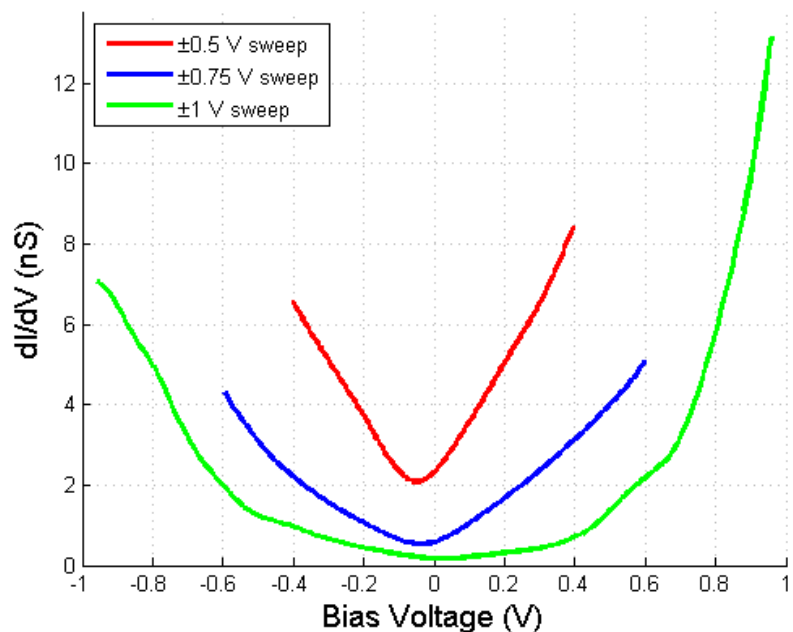
Figure 5.1: Averaged tunneling spectra on clean HOPG over different voltage ranges. Tip-sample distance was fixed before each acquisition by setting $V = -0.5, -0.75$, or -1 V and $I = 100$ pA.

the grid. These could then be grouped by their corresponding topography. Multiple curves from the same type of surface region (*e.g.*, a particular TMA phase) were averaged together and smoothed by convolution with a Gaussian 0.1 eV wide, since narrower features would most likely be the result of thermal fluctuations. Averaged spectra were then numerically differentiated to obtain dI/dV as a function of V, which provides information about the electronic density of states as discussed in Section 2.2.

5.1 Bare HOPG(0001) characterization

The first step in these experiments was to establish a baseline for curves on HOPG. STS is known to vary with the bias voltage range and tip-sample separation [57, 59]. Therefore, spectra were obtained in several configurations as shown in Figure 5.1.

Each dI/dV curve shows the characteristic V-shape expected on graphite [18, 112]. The electron (right) and hole (left) conduction portions of the curves are slightly asymmetric and the minimum points range from -0.05 to 0.03 V (analogous to the Dirac point in graphene). The ± 1 V sweep is dominated by conductance at higher voltage magnitudes, providing less information near the minimum point which is of greatest interest for gap engineering applications. Subsequent spectra on TMA films were taken over $|V| \leq 500$ meV, comparable to the red curve in Figure 5.1.

5.2 STS of TMA structural phases

Tunneling spectra from different phases of TMA may be effectively compared by sampling in a grid over a relatively wide scan area that incorporates the relevant phases. In this way, all curves can be certain to have been acquired under very similar tip conditions. Figure 5.2 contains one such STM image with honeycomb (H_1), flower (H_2), and smooth (2D gas) regions, along with their associated spectra. 256-576 individual I-V curves were averaged to create each dI/dV spectrum.

Figure 5.3's comparison of the dI/dV curve from the "smooth" area in Figure
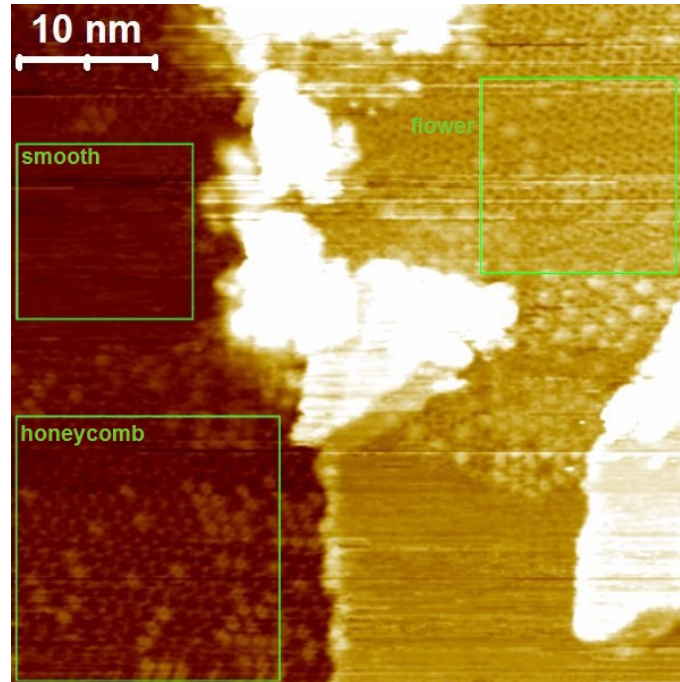
(a)
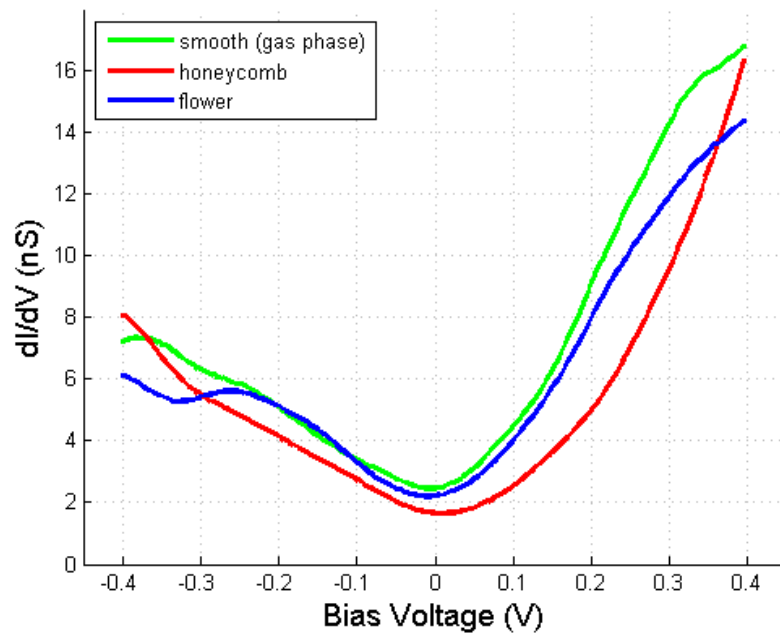
(b)

Figure 5.2: (a) STM image taken immediately after a 48×48 STS grid over the same area. Regions for averaging are marked in green. (b) Tunneling spectra corresponding to each region.

5.2 to the $|V| \leq 0.5$ V sweep from Figure 5.1 confirms that the region is not clean graphite. It displays a much more pronounced electron-hole asymmetry and a shift of $+0.04$ V in the minimum conductance. This supports the conclusion, presented in the previous chapter, that many apparently-flat regions of these samples after TMA deposition contain a highly mobile 2D gas.

In fact, all three spectra from different TMA phases show similar features. Figure 5.4 shows each dI/dV curve from Figure 5.2 after subtraction of the spectrum from HOPG over the same voltage range. Given the proportionality between dI/dV and DOS, these residuals can be attributed to the change in electron states as a result of the presence of TMA. The higher density of states for positive voltages is likely a signature of the TMA LUMO near the graphite E_F as calculated in Ref. [51]. The honeycomb curve shows DOS depletion near 0 V, which is a promising indication for band gap opening. However, these spectra have limited resolution in V as a result of thermal noise and film instability, so more definite conclusions cannot be drawn until further data is gathered.

5.3   STS of filled host/guest structures

The annealed sample with near-100% guest molecule filling, discussed in Section 4.2, did not exhibit the same instability problems as most other films. An STS grid acquired over a scan area with both H_1 and H_2 networks resulted in the dI/dV curves plotted in Figure 5.5. Variances in both the I-V curves used in averaging was a factor of 4 smaller than the variances for all three spectra presented in the
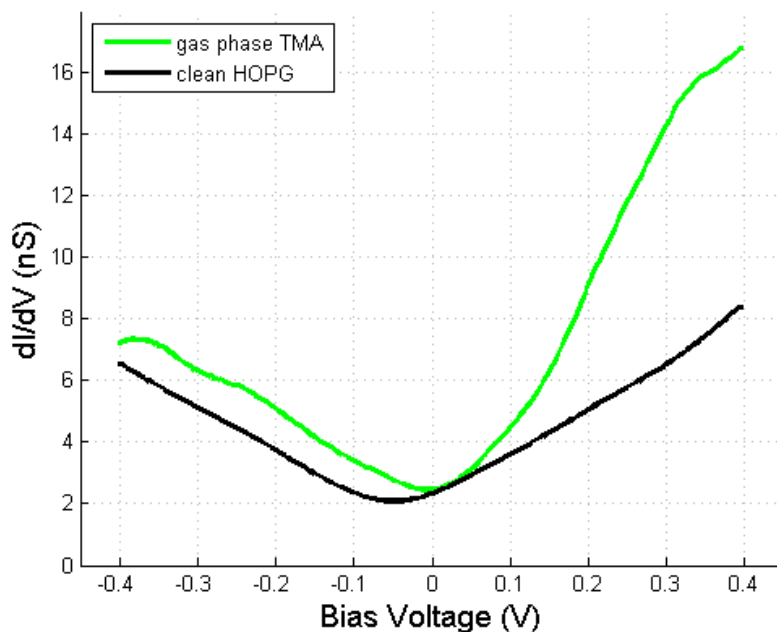
Figure 5.3: STS from TMA in gas phase is distinct from spectra taken on clean graphite.

previous section.

Unlike in the as-grown sample, the tunneling spectra corresponding to honeycomb and flower TMA networks in the annealed sample are nearly identical. Both curves were well-fit by a parabola plus a Gaussian peak; the only significantly different fitting parameter corresponded to the height of the peak at 4.47±0.02 nS for H_1 and 4.20±0.02 nS for H_2. This peak, at −0.14 V, is the most striking difference between this and the previous set of spectra. (A smaller feature at the same voltage may have been present, especially in the flower curve, but is difficult to distinguish given the stability issues.)

To what can this peak be attributed? The most obvious structural difference between the films is the concentration of guest molecules inside network pores. In
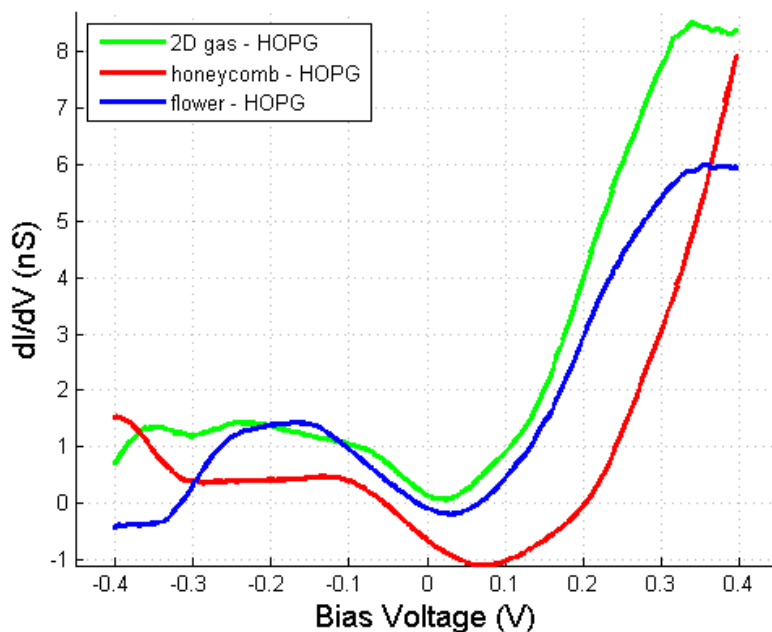
Figure 5.4: STS data from Fig. 5.2 after the HOPG baseline was subtracted.

the as-grown sample, only approximately 1/4 of host sites are filled. Guest molecules may contribute electronic states accessible at -0.14 V, resulting in a stronger signal at that voltage in the annealed film. However, one would expect significantly different results on the honeycomb versus flower phases, since H_1 contains one pore per 1.4 nm^2 while H_2 contains one per 3.6 nm^2. The dI/dV peak in the honeycomb phase is indeed higher than in the flower phase, but only by six percent. Guest molecule concentration alone cannot explain this observation, since even in the fully-filled annealed film the concentrations differ by a factor of 2.5. Perhaps it is the completion of a periodic host/guest network structure, rather than simply the number of guest molecules, that is most important to the DOS. Future STS measurements may allow this question to be answered more decisively.
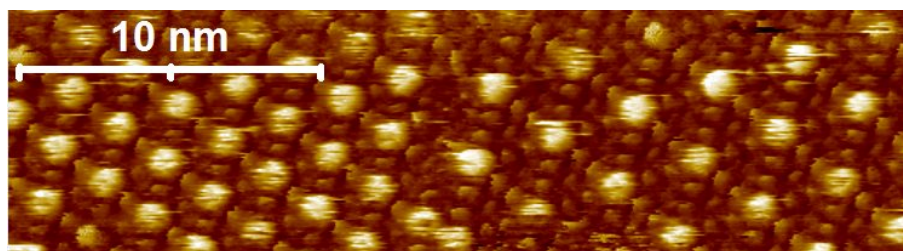
(a)
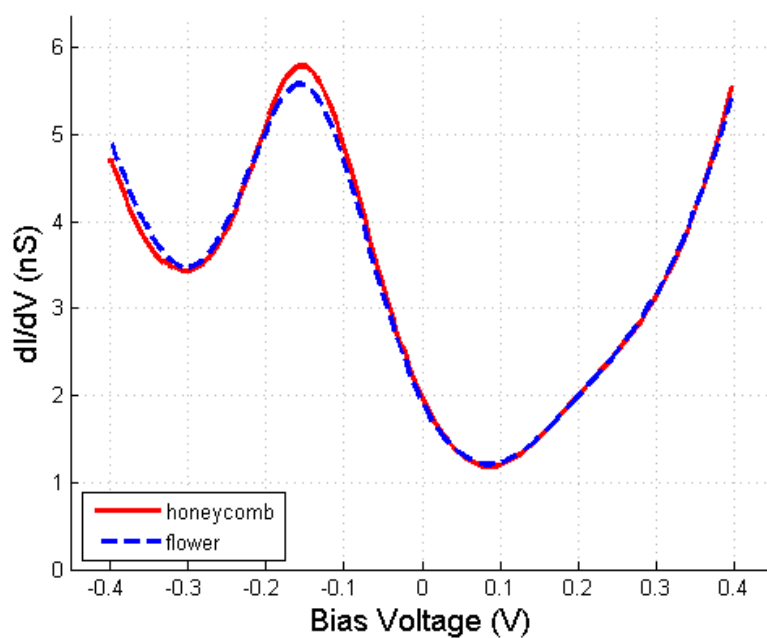
(b)

Figure 5.5: (a) Portion of an STM image taken immediately after a 48×48 STS grid on annealed TMA/HOPG sample, showing near-complete pore filling with guest molecules. (b) Tunneling spectra comparing data from H_1 (left side of image) and H_2 (right side of image).

5.4 Discussion

Scanning tunneling spectroscopy has been performed on TMA networks on graphite. These room-temperature, UHV measurements are the first look at a rich and complex electronic system, and accordingly they raise more questions than they answer. Additional exploration of this system is warranted to discover more about the electronic properties of molecular thin films and layered structures, as well as to develop promising methods for graphene band structure engineering.

The observed depletion of states near $V = 0$ in H_1 TMA on graphite is an early indication that ordered TMA lattices are an effective way to open a gap in graphene. (Density functional theory calculations [111] for the appropriate registry of TMA on graphene have also confirmed symmetry-breaking and gap creation.) A better understanding of the apparent state at -0.14 V in filled host/guest structures also deserves consideration for device applications, since guest TMA molecules are a persistent presence in these films.

Gathering more I-V curves would at least provide better statistics, in principle resulting in averaged spectra that are more representative of the real DOS. Unfortunately, obtaining large amounts of STS data that could be confidently associated with identifiable topographic features was prohibitively difficult in this study. The low coverage of ordered networks and tendency for observed networks, once found, to suddenly disperse into the gas phase—already significant challenges for topographic measurements–posed extra hurdles to spectroscopy, since the STM images taken immediately before and after an STS grid acquisition could look drastically

different. If tunneling spectra could not be attributed to a particular film phase, they were deemed unreliable and rejected from this analysis.

Future STS on cold samples could provide greater insight through higher energy resolution and improved film stability. Low-temperature measurements could also enable spatially-resolved STS, providing a better understanding of how various parts of the TMA lattice contribute to the final density of states. Improved film growth procedures, discussed in Section 4.4, might assist in creating networks that are stable enough over long timescales to allow better STS feature resolution even without cooling.

Chapter 6

Thesis summary and conclusions

In the preceding chapters I have examined the nucleation behavior of C_{60} on ultrathin SiO_2 and the morphological and electronic properties of trimesic acid on graphite. Each of these systems provides an elegant window into basic phenomena of surface physics, including the interplay between molecule-substrate and intermolecular interactions, the effects of surface impurities or defects, and molecular self-assembly. Additionally, both systems are relevant to nanotechnology applications. Through this work, I have sought to further our ability to engineer nanostructures with ideal properties, by enhancing our understanding of the physics that governs those properties.

The earliest nucleation stages of C_{60} on ultrathin oxide were quantified using capture zone analysis of scanning tunneling microscopy images. Individual C_{60} molecules were resolved with STM. Monomer "islands" were the predominant species at 0.1 monolayer coverage, though larger clusters of up to a dozen or more molecules were also observed. After performing physical vapor deposition of C_{60} at five different substrate temperatures and imaging the resulting films with STM, capture zones were drawn for the measured islands and CZ area distributions were tabulated. These distributions were fit by the generalized Wigner distribution and the gamma distribution so that the critical nucleus size i could be extracted from fitting

parameters. Both GWD and ΓD were found to fit the CZ area distributions equally well.

The value of i in this system was found to vary with temperature. This variation was not simply an increase with temperature as expected, but was instead parabolic, first increasing up to $\sim 386 \pm 3$ K and then decreasing again. The temperature-dependence may be understood as a signature of varying oxide binding sites acting like defects or impurities on the surface. Increasing in strength with rising temperature, these defects eventually overwhelm the homogeneous nucleation process and return the system to an $i = 0$ state. Since the grain size in thicker, device-applicable films is related to the system's value of i during initial nucleation, this result could allow grain size tuning in a C_{60}/SiO_2 growth procedure.

Hexagonal porous networks of trimesic acid on highly-oriented pyrolitic graphite were also measured using scanning tunneling microscopy. The first reported STM images of these networks in room-temperature UHV were achieved, though film stability issues still pose a significant hurdle to data acquisition. Phases H_1 (honeycomb, 2-molecule unit cell) and H_2 (flower, 6-molecule unit cell) were by far the most prevalent, though grains with networks up to H_7 were also observed. Any of these 2D TMA lattices have the potential to break the graphene sublattice degeneracy if in the appropriate registry with a graphene substrate, opening a band gap and allowing graphene+TMA structures to be used in transistor applications.

Tunneling spectroscopy measurements of the TMA/HOPG system were also undertaken to begin establishing expectations for how TMA networks could influence the graphene density of states. Since STS dI/dV features are closely related to

DOS features, STS can be a useful tool to investigate the appearance of electronic states associated with certain crystal features, or the depletion of electronic states indicating the presence of a band gap. STS measurements performed in this thesis show the emergence of a peak at -0.14 V associated with near-complete filling of TMA's hexagonal pores with excess TMA guest molecules. They also indicate significant changes to the graphite DOS in the presence of TMA networks; higher-resolution spectra on more stable films are needed to establish the exact character of these changes.

The deposition of self-ordering molecular adsorbate films appears to be a promising technique for graphene band structure engineering. Future studies with other molecules and on graphene itself are of course necessary to make progress with this method, but based on the results described here and theoretical simulations by other members of our research group, I anticipate that those studies will eventually bear fruit.

Appendix A

Code for capture zone analysis

A.1 Inputs

The code below requires as input the results of running SPIP Particle and Pore Analysis on an STM topography image. Height threshold, maximum and minimum particle sizes, and other attributes may be set in order to ensure that the software correctly identifies islands of interest. Only the output parameters "Area," "X Geometric Center," and "Y Geometric Center" should be selected and saved as a text file. All header rows should be deleted. For each island, these three values and the automatically-included particle ID are read in and used for Voronoi cell calculations.

A.2 vor.pro

This function makes use of a built-in IDL routine to compute Voronoi cells, `voronoi.pro`, found in IDL's `lib` directory. Specifically, it calls `VORONOI_B`, a version of the built-in routine which has been modified to output the array (`ext`) specifying which points are "internal" and which are "external." This code is written for X-window graphics devices, typically used in Unix-based operating systems. An earlier version of this code was used in Ref. [12] and included in Ref. [113].

```
pro vor, isize
;isize is the size of the image in um
;ex: 20umx20um image would be entered vor, 20

;Define the data directory
DEFSYSV, '!DATA_DIR', '/home/michelle/IDL/data/'

;Define variables
Total_Area = 0.00
ext = 0
isizenm = isize*1000

;Create SaveName variable
LongSaveName = DIALOG_PICKFILE(PATH=!DATA_DIR, /READ)
Print, 'data=', LongSaveName
pos1 = STRPOS(LongSaveName, '/data/')
rawfilename = STRMID(LongSaveName, pos1+6)

Print, "rawfilename=",rawfilename

;Save data in Spread format
savefolder = '/home/michelle/IDL/data/saveddata/'
savename = STRCOMPRESS(savefolder + rawfilename + '.txt')
Print,'savename = ', savename

SET_PLOT, 'PS'
vorsavename = STRCOMPRESS(savefolder + rawfilename + '.vor' +'.ps')
DEVICE, FILENAME=vorsavename, /inches, xsize = 6.0, ysize = 6.0
plot, [0,isizenm], [0,isizenm], /nodata, XTITLE="Distance (nm)",
YTITLE="Distance (nm)", TITLE = "Voronoi Plot"

;read in file
data = READ_ASCII(LongSaveName)

;tIarea = data.field01[2,*]
tIarea = data.field1[1,*]
W = data.field1[0,*]
W = UINT(W)
;X = data.field01[32,*]
;Y = data.field01[33,*]
X = data.field1[2,*]
Y = data.field1[3,*]

Iarea = ABS(TRANSPOSE(tIarea))
```

```
;put x and y in terms of a origin of 0,0 system
X = X + isizenm/2
Y = Y + isizenm/2

;sort data, delete duplicate points
GRID_INPUT, X, Y, W, X_Sorted, Y_Sorted, tw_sorted
w_sorted = TRANSPOSE(tw_sorted)

; Triangulate the points:
TRIANGULATE, X_Sorted, Y_Sorted, tr, CONN=C
N = N_ELEMENTS(X_Sorted)
CZarea = DBLARR(N)
sorted_Iarea = DBLARR(N)
ext_list = INTARR(N)

;Voronoi loop
   FOR I0=0, N-1 DO BEGIN
      VORONOI_B, X_Sorted, Y_Sorted, I0, C, Xp, Yp, rec, ext
      ;capture ext...remember if points are interrior or exterior
      ext_list[I0] = ext
      ;Extra interior/exterior conditions beyond voronoi
      N2 = N_ELEMENTS(Xp)
      FOR I1 = 0, N2-1 DO BEGIN
         ;Print, "I1=", I1
         IF Xp[I1] le 0 THEN BEGIN
            ext_list[I0] = UINT(1)
            ;Print, "Xp[",I1,"] is le 0"
         ENDIF
         IF Xp[I1] ge isizenm THEN BEGIN
            ext_list[I0] = UINT(1)
            ;Print, "Xp[",I1,"] is ge isizenm"
         ENDIF
         IF Yp[I1] le 0 THEN BEGIN
            ext_list[I0] = UINT(1)
            ;Print, "Yp[",I1,"] is le 0"
         ENDIF
         IF Yp[I1] ge isizenm THEN BEGIN
            ext_list[I0] = UINT(1)
            ;Print, "Yp[",I1,"] is ge isizenm"
         ENDIF
      ENDFOR
      ext = ext_list[I0]
      ; Find the Areas:
      A = POLY_AREA(Xp,Yp)
      ;Save the areas in an array
```

```
      CZarea[I0] = A
      ; Draw it:
      IF EXT eq 0 THEN POLYFILL, Xp, Yp, CLIP=[0,0,isizenm,isizenm],
      COLOR = 70+I0*8, THICK=2, /data, NOCLIP=0
      IF EXT eq 0 THEN BEGIN
      PLOTS, Xp, Yp, /data
      PLOTS, Xp, Yp, /data, THICK=4.0, /CONTINUE
      ENDIF
   ENDFOR

;Plot the centers of masses on polyfill graph
oplot, X_Sorted, Y_Sorted, Psym=3, SYMSIZE=4.0
Device, /CLOSE_FILE
SET_PLOT, 'x'

   FOR I0=0, N-1 DO BEGIN
      ;Find value of zone index in sorted data in position I0
      I1 = w_Sorted[I0]
      ;where is I1 in the unsorted data?
      I2 = WHERE(W EQ I1)
      ;Make a sorted array for Iarea
      ;using the same mapping as GRID_INPUT uses
      sorted_Iarea[I0] = Iarea[I2]
   ENDFOR

;make list of positions, area, etc of interior locations only
M = UINT(Total(ext_list))
P = N-M
Interior_ext = INTARR(P)
Interior_CZarea = DBLARR(P)
N1 = 0
Interior_X = DBLARR(P)
Interior_Y = DBLARR(P)
Interior_I_size = DBLARR(P)

   FOR I0=0, N-1 DO BEGIN
      IF ext_list[I0] eq 0 THEN BEGIN
         Interior_CZarea[N1] = CZarea[I0]
         Interior_X[N1] = X_Sorted[I0]
         Interior_Y[N1] = Y_Sorted[I0]
         Interior_I_Size[N1] = sorted_Iarea[I0]
         N1 = N1 + 1
      ENDIF
   ENDFOR
```

```
Window, 4, retain = 2, XSIZE = 512, YSIZE = 512, title="Interior
Voronoi Plot"
plot, [0,isizenm], [0,isizenm], /nodata
plot, X_Sorted, Y_Sorted, Psym=5
Wait, 1
oplot, Interior_X, Interior_Y, Psym = 5, color = 120

;Plot a Histogram in a different window (2):
Window, 2, Retain=2, title="Interior CZ Area Histogram"

;Define an area bin size
;binsize = 10000
binsize = 10

;Define a histogram max
;hmax = 1000000
hmax = 500

;give me the smallest area in long form:
start = long(min(Interior_CZarea)/binsize) * binsize
histog = histogram(Interior_CZarea,binsize=binsize,min=start,max=hmax)

;Find how many elements in density
number_unique = n_elements(histog)

;pad with zeros
vis_histog = fltarr(number_unique+2)
vis_histog(1:number_unique) = histog
xaxis = (findgen(number_unique+2)-.5)*binsize
plot,xaxis,vis_histog,psym=10, XTITLE="Interior CZArea", YTITLE="Frequency
(No units)", /data, title="CZArea Histogram"

;save histogram
SET_PLOT, 'PS'
hsavename = STRCOMPRESS(savefolder + rawfilename + '.hist' +'.ps')
DEVICE, FILENAME=hsavename
plot,xaxis,vis_histog,psym=10, XTITLE="Interior CZArea", YTITLE="Frequency
(No units)", /data, title="CZArea Histogram"
Device, /CLOSE_FILE
SET_PLOT, 'x'

;Plot Capture Zone Area Vs Island Size
Window, 3, retain = 2, XSIZE = 512, YSIZE = 512, title="Interior Capture
Zone Area Vs. Island Area"
;plot, [0,isizenm], [0,isizenm], /nodata
```

```
; Define max yrange, previously 1000000
yrange = hmax
Plot, Interior_I_size, Interior_CZArea, Psym=5, YRANGE=[0,yrange], XTITLE
="Island_Area", YTITLE="CZ_Area", title="Interior Capture Zone Area Vs.
Island Area"

;save capture zone vs island size plot
SET_PLOT, 'PS'
czsavename = STRCOMPRESS(savefolder + rawfilename + '.cz' +'.ps')
DEVICE, FILENAME=czsavename
Plot, Interior_I_size, Interior_CZArea, Psym=5, YRANGE=[0,yrange], XTITLE=
"Island_Area", YTITLE="CZ_Area", title="Interior Capture Zone Area Vs.
Island Area"
Device, /CLOSE_FILE
SET_PLOT, 'x'

;save all the data
OpenW, /APPEND, 10, savename
printf, 10, SYSTIME(0)
;Units: Xpos(nm), Ypos(nm), Interior_I_size(nm^2), Interior_CZArea(nm^2)
printf, 10, '  Xposition  ','  Yposition  ','Island_Size',
'CaptureZoneArea'
   For i = 0, P-1 Do Begin
      printf, 10, Interior_X[i], Interior_Y[i], Interior_I_Size[i],
      Interior_CZarea[i]
   EndFor

Close, 10

End
```

A.3   Outputs

This code creates several plots on-screen and saves corresponding PostScript
files as well as a text file containing the X position, Y position, island size, and
capture zone area for all capture zones found. In this thesis, the text file data
was subsequently loaded into and processed with MATLAB. The PostScript files
generated are:
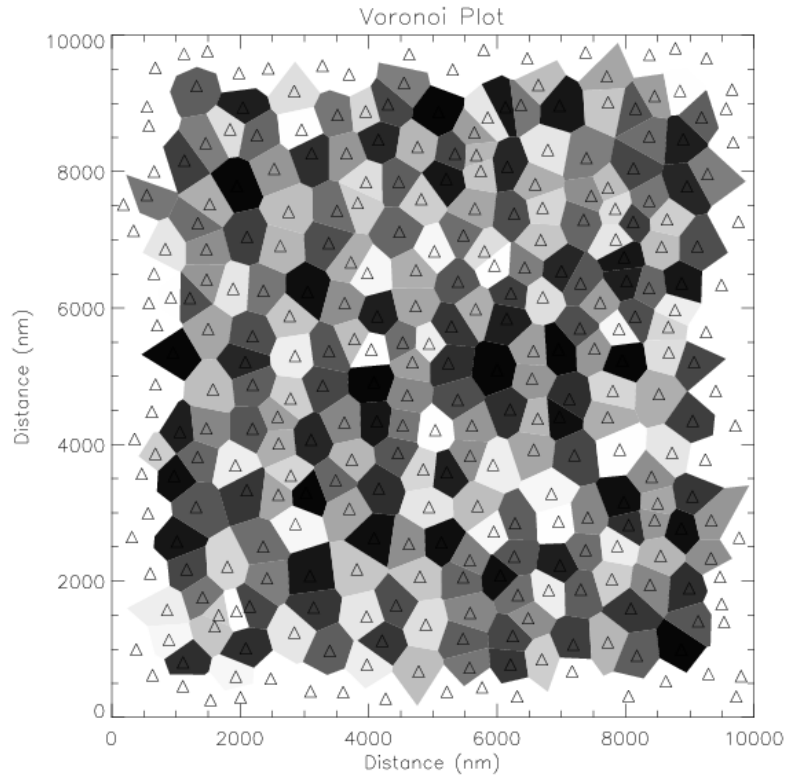
Figure A.1: Example Voronoi diagram created by IDL code.

- `[input filename].cz.ps`, a scatterplot of interior capture zone area versus island area

- `[input filename].hist.ps`, a histogram of capture zone areas

- `[input filename].vor.ps`, a shaded Voronoi diagram of capture zones with island centers marked

An example of the final plot is shown in Figure A.1.

Appendix B

Code for STS analysis

This appendix contains MATLAB functions used for averaging and differentiating scanning tunneling spectroscopy data. Occasionally, linebreaks not compatible with MATLAB syntax have been added to fit a single line of code on a printed page; therefore, the reader interested in using these functions should be wary of simply copying and pasting the text here. All functions were written and executed in MATLAB R2008b Student Edition. Used in combination, these functions can be used to create plots like the ones shown in Chapter 5.

B.1   Inputs

Saved STS line or grid data files opened in the Nanonis Binary File Inspector can be directly re-saved into a text-based format. In the Export box, select "Point Spectro." and export as ASCII. The code below assumes that the tunneling spectrum data from all points in a given line or grid are located within a folder and named using the convention `[folder name]-PointSpec[5-digit number].dat`.

B.2   MATLAB functions

The function `readSTSfile` takes two inputs: a string path name and an integer number corresponding to the number of points in a spectral sweep. It returns three

columns of data (V plus forward and backward I) from the STS ASCII file.

```
function f = readSTSfile(path,numpts)
    fid = fopen(path,'r');
    data = textscan(fid,'%f',numpts*3,'HeaderLines',15);
    data = data{:};

    % arrange data into columns for easily understandable access
    newdata = zeros(numpts,3);
    count=1;
    for r=1:numpts;
        newdata(r,:)=data(count:count+2);
        count = count+3;
    end

    fclose(fid);
    f = newdata;
end
```

The function `dIdV` takes V and I data from an STS curve, then outputs dI/dV and a new V trimmed to account for endpoint artifacts resulting from numerical differentiation.

```
function [v,f] = dIdV(vsweep,isweep)
% our bias configuration is opposite convention
vsweep = -vsweep;
% calculate V per pixel
vpp = (max(vsweep)-min(vsweep))/length(vsweep);
minfeature = .1;
smooth = floor(2*minfeature/vpp);

% first smooth the current data
% smooth using convolution with gaussian
window = gausswin(smooth);
newi = conv(isweep,window);
isweep = newi(1+floor((smooth-1)/2):length(newi)-ceil((smooth-1)/2));

% the curve we just made will have weird edge effects. trim:
vsweep = vsweep(ceil(smooth/2):256-ceil(smooth/2));
isweep = isweep(ceil(smooth/2):256-ceil(smooth/2));

% then compute derivative
```

```
deriv = zeros(size(isweep));
if (vsweep(1)<vsweep(length(vsweep)))
    for idx = 1:length(isweep)
        if idx==1
            deriv(idx) = (isweep(idx+2)-isweep(idx))/(vsweep(idx+2)
            -vsweep(idx));
        elseif idx==length(isweep)
            deriv(idx) = (isweep(idx)-isweep(idx-2))/(vsweep(idx)
            -vsweep(idx-2));
        else deriv(idx) = (isweep(idx+1)-isweep(idx-1))/(vsweep(idx+1)
        -vsweep(idx-1));
        end
    end
else
    for idx = length(isweep):-1:1
        if idx==1
            deriv(idx) = (isweep(idx)-isweep(idx+2))/(vsweep(idx)
            -vsweep(idx+2));
        elseif idx==length(isweep)
            deriv(idx) = (isweep(idx-2)-isweep(idx))/(vsweep(idx-2)
            -vsweep(idx));
        else deriv(idx) = (isweep(idx-1)-isweep(idx+1))/(vsweep(idx-1)
        -vsweep(idx+1));
        end
    end
end
f = deriv;
v = vsweep;
end
```

The function `processSTS` is for linecut data. It takes the folder name, number of

points in the line, and distance in nanometers spanned by the line. It returns a

voltage axis vector and an array of all the current data in the line. It also generates

a filled contour plot for visualization of the tunneling spectrum as a function of

position.

```
function [Vaxis,f] = processSTS(filename,numpts,width)
% filename is prefix to numbered STS files
% width in nm
```

```matlab
toplot = zeros(256,numpts);
Vaxis = zeros(256,1);

% import data from all points in linecut
for idx = 1:numpts
    % create filename
    numstr = '000';
    if idx<10
        numstr = strcat(numstr,'0',num2str(idx));
    else numstr = strcat(numstr,num2str(idx));
    end
    thisfile = strcat(filename,'/',filename,'-PointSpec',numstr,'.dat');
    %save data into array
    newdata = readSTSfile(thisfile,256);
    toplot(:,idx) = newdata(:,2);
    Vaxis = newdata(:,1);
end

rows = Vaxis;
colstep = width/numpts;
cols = colstep:colstep:width;
[X,Y] = meshgrid(cols,rows);

figure();
hold on;
contourf(X,Y,toplot,25,'LineStyle','none')
title(filename);
xlabel('position (nm)');
ylabel('bias voltage (V)');
colorbar;

f = toplot;
end
```

The function `stdevSTS` is similar to the previous function but designed for grid spectroscopy. It also takes a folder name string and a number corresponding to the size of the grid (assumed to be square, `numpts`×`numpts`), but then requires the integer (x,y) grid coordinates for the first and last spectra in the desired region. MATLAB's image display conventions have flipped the data vertically but *not* hor-

izontally, compared to the view one would see in the Nanonis Binary File Inspector or Scan Inspector programs, so special care must be taken in selecting these coordinates. The function returns three vectors: voltage, current averaged over the region, and standard deviation of the current values.

```
function [v,i,s] = stdevSTS(filename,numpts,beginx,beginy,endx,endy)
toAverage = zeros(256,endx-beginx+1,endy-beginy+1);
% 3D: 256 rows, x sampling range columns, y sampling range depth

bias = zeros(256,1);
biasyet = 0;
count2 = 0;
for idx1 = beginy:endy
    count1 = idx1-beginy+1;
    for idx2 = (idx1-1)*numpts+1:idx1*numpts
        count2=count2+1;
        if (count2>=beginx)&&(count2<=endx)
            % create filename
            if idx2<10
                numstr = strcat('0000',num2str(idx2));
            elseif idx2<100
                numstr = strcat('000',num2str(idx2));
            elseif idx2<1000
                numstr = strcat('00',num2str(idx2));
            else numstr = strcat('0',num2str(idx2));
                % this is sufficient as long as numpts<100
            end
            thisfile = strcat(filename,'/',filename,'-PointSpec',
            numstr,'.dat');
            %save data into array
            newdata = readSTSfile(thisfile,256);
            if biasyet==0
                bias = newdata(:,1);
                biasyet = 1;
            end
            toAverage(:,count2-beginx+1,count1) = newdata(:,2);
        end
    end
    count2=0;
end

aveSTS = sum(sum(toAverage,3),2)./((endy-beginy+1)*(endx-beginx+1));
```

```
% compute std dev
toSubtract = ones(size(toAverage));
for xidx = 1:endx-beginx+1
    for yidx = 1:endy-beginy+1
        toSubtract(:,xidx,yidx)=aveSTS;
    end
end
temp = (toAverage - toSubtract).^2;
sigma2 = sum(sum(temp,3),2)./((endy-beginy+1)*(endx-beginx+1));
sigma = sigma2.^(1/2);
i = aveSTS;
s = sigma;
v = bias;
end
```

Bibliography

[1] J.A. Venables, G.D.T. Spiller, and M. Hanbucken. Nucleation and growth of thin films. *Rep. Prog. Phys.*, 47(4):399, 1984.

[2] S.R. Forrest. Ultrathin Organic Films Grown by Organic Molecular Beam Deposition and Related Techniques. *Chem. Rev.*, 97:1793–1896, 1997.

[3] Z. Zhang and M.G. Lagally. Atomistic processes in the early stages of thin-film growth. *Science*, 276(5311):377–383, 1997.

[4] D.S. Germack, C.K. Chan, B.H. Hamadani, L.J. Richter, D.A. Fischer, D.J. Gundlach, and D.M. DeLongchamp. Substrate-dependent interface composition and charge transport in films for organic photovoltaics. *Appl. Phys. Lett.*, 94(23):233303, 2009.

[5] S.S. Lee and Y.-L. Loo. Structural complexities in the active layers of organic electronics. *Ann. Rev. Chem. Biomol. Eng.*, 1:59–78, 2010.

[6] O.D. Jurchescu, D.A. Mourey, S. Subramanian, S.R. Parkin, B.M. Vogel, J.E. Anthony, T.N. Jackson, and D.J. Gundlach. Effects of polymorphism on charge transport in organic semiconductors. *Phys. Rev. B*, 80(8):085201, 2009.

[7] P.F. Green. The Green Group: Organic Electronics (web page). `http://www.greengroup.engin.umich.edu/electronics.html`, June 2013.

[8] I. Salzmann, S. Duhm, R. Opitz, R.L. Johnson, J.P. Rabe, and N. Koch. Structural and electronic properties of pentacene-fullerene heterojunctions. *J. Appl. Phys.*, 104(11):114518–114518, 2008.

[9] M. Avrami. Granulation, Phase Change, and Microstructure: Kinetics of Phase Change. III. *J. Chem. Phys.*, 9:177, 1941.

[10] D. Walton. Nucleation of vapor deposits. *J. Chem. Phys.*, 37:2182, 1962.

[11] C. Ratsch, A. Zangwill, P. Šmilauer, and D.D. Vvedensky. Saturation and scaling of epitaxial island densities. *Phys. Rev. Lett.*, 72(20):3194–3197, 1994.

[12] B.R. Conrad, E. Gomar-Nadal, W.G. Cullen, A. Pimpinelli, T.L. Einstein, and E.D. Williams. Effect of impurities on pentacene island nucleation. *Phys. Rev. B*, 77:205328, 2008.

[13] A.K. Geim and K.S. Novoselov. The rise of graphene. *Nat. Mater.*, 6(3):183–191, 2007.

[14] PR Wallace. The band theory of graphite. *Phys. Rev.*, 71(9):622, 1947.

[15] R. Saito, G. Dresselhaus, and M.S. Dresselhaus. *Physical properties of carbon nanotubes.* Imperial College Press London, 1998.

[16] S.Y. Zhou, G.-H. Gweon, A.V. Fedorov, P.N. First, W.A. De Heer, D.-H. Lee, F. Guinea, A.H. Castro Neto, and A. Lanzara. Substrate-induced bandgap opening in epitaxial graphene. *Nat. Mater.*, 6(10):770–775, 2007.

[17] V.W. Brar, Y. Zhang, Y. Yayon, T. Ohta, J.L. McChesney, A. Bostwick, E. Rotenberg, K. Horn, and M.F. Crommie. Scanning tunneling spectroscopy of inhomogeneous electronic structure in monolayer and bilayer graphene on sic. *Appl. Phys. Lett.*, 91(12):122102, 2007.

[18] P. Lauffer, K.V. Emtsev, R. Graupner, T. Seyller, L. Ley, S.A. Reshanov, and H.B. Weber. Atomic and electronic structure of few-layer graphene on SiC(0001) studied with scanning tunneling microscopy and spectroscopy. *Phys. Rev. B*, 77(15):155426, 2008.

[19] E. McCann. Asymmetry gap in the electronic band structure of bilayer graphene. *Phys. Rev. B*, 74:161403, 2006.

[20] B.E. Feldman, J. Martin, and A. Yacoby. Broken-symmetry states and divergent resistance in suspended bilayer graphene. *Nat. Phys.*, 5(12):889–893, 2009.

[21] T. Ohta, A. Bostwick, T. Seyller, K. Horn, and E. Rotenberg. Controlling the electronic structure of bilayer graphene. *Science*, 313(5789):951–954, 2006.

[22] Y. Zhang, T.-T. Tang, C. Girit, Z. Hao, M.C. Martin, A. Zettl, M.F. Crommie, Y.R. Shen, and F. Wang. Direct observation of a widely tunable bandgap in bilayer graphene. *Nature*, 459:820–823, 2009.

[23] H. Min, B. Sahu, S.K. Banerjee, and A.H. MacDonald. *Ab initio* theory of gate induced gaps in graphene bilayers. *Phys. Rev. B*, 75:155115, 2007.

[24] Z.H. Ni, T. Yu, Y.H. Lu, Y.Y. Wang, Y.P. Feng, and Z.X. Shen. Uniaxial strain on graphene: Raman spectroscopy study and band-gap opening. *Nano*, 2(11):2301–2305, 2008.

[25] Z.H. Ni, T. Yu, Y.H. Lu, Y.Y. Wang, Y.P. Feng, and Z.X. Shen. Uniaxial strain on graphene: Raman spectroscopy study and band-gap opening (correction). *Nano*, 3(2):483–483, 2009.

[26] V.M. Pereira, A.H. Castro Neto, and N.M.R. Peres. Tight-binding approach to uniaxial strain in graphene. *Phys. Rev. B*, 80(4):045401, 2009.

[27] G. Cocco, E. Cadelano, and L. Colombo. Gap opening in graphene by shear strain. *Phys. Rev. B*, 81(24):241412, 2010.

[28] F. Guinea, M.I. Katsnelson, and A.K. Geim. Energy gaps and a zero-field quantum Hall effect in graphene by strain engineering. *Nat. Phys.*, 6(1):30–33, 2009.

[29] N. Levy, S.A. Burke, K.L. Meaker, M. Panlasigui, A. Zettl, F. Guinea, A.H. Castro Neto, and M.F. Crommie. Strain-induced pseudo-magnetic fields greater than 300 Tesla in graphene nanobubbles. *Science*, 329(5991):544–547, 2010.

[30] G. Giovannetti, P.A. Khomyakov, G. Brocks, P.J. Kelly, and J. van den Brink. Substrate-induced band gap in graphene on hexagonal boron nitride: *Ab initio* density functional calculations. *Phys. Rev. B*, 76(7):073103, 2007.

[31] M. Yankowitz, J. Xue, D. Cormode, J.D. Sanchez-Yamagishi, K. Watanabe, T. Taniguchi, P. Jarillo-Herrero, P. Jacquod, and B.J. LeRoy. Emergence of superlattice Dirac points in graphene on hexagonal boron nitride. *Nat. Phys.*, 8(5):382–386, 2012.

[32] L.A. Ponomarenko, R.V. Gorbachev, G.L. Yu, D.C. Elias, R. Jalil, A.A. Patel, A. Mishchenko, A.S. Mayorov, C.R. Woods, J.R. Wallbank, M. Mucha-Kruczynski, B.A. Piot, M. Potemski, I.V. Grigorieva, K.S. Novoselov, F. Guinea, V.I. Fal'ko, and A.K. Geim. Cloning of Dirac fermions in graphene superlattices. *Nature*, 497(7451):594–597, 2013.

[33] B. Hunt, J.D. Sanchez-Yamagishi, A.F. Young, M. Yankowitz, B.J. LeRoy, K. Watanabe, T. Taniguchi, P. Moon, M. Koshino, P. Jarillo-Herrero, and R.C. Ashoori. Massive Dirac Fermions and Hofstadter Butterfly in a van der Waals Heterostructure. *Science*, 340(6139):1427–1430, 2013.

[34] C.R. Dean, L. Wang, P. Maher, C. Forsythe, F. Ghahari, Y. Gao, J. Katoch, M. Ishigami, P. Moon, M. Koshino, T. Taniguchi, K. Watanabe, K.L. Shepard, J. Hone, and P. Kim. Hofstadter's butterfly and the fractal quantum Hall effect in moiré superlattices. *Nature*, 497(7451):598–602, 2013.

[35] H. Wiechert, E. Maus, and K. Knorr. Dielectric and Structural Studies of Trifluoromethane Monolayers on Boron Nitride and Graphite. *Jap. J. Appl. Phys. Supplement*, 26(3):889–890, 1987.

[36] D. Arndt and K. Knorr. Heat capacity study of CF_3H physisorbed on graphite. *Mol. Phys.*, 95(1):91–96, 1998.

[37] K. Knorr, S. Fassbender, A. Warken, and D. Arndt. Melting of Monolayers of Some Halomethanes and Haloethanes Physisorbed on Graphite. *J. Low Temp. Phys.*, 111(3-4):339–348, 1998.

[38] P. Thomas, Y. Xia, D.A. Boyd, T.A. Hopkins, and G.B. Hess. Study of SF_6 adsorption on graphite using infrared spectroscopy. *J. Chem. Phys.*, 131:124709, 2009.

[39] Y. Wang, W. Bao, S. Xiao, M. Fuhrer, and J. Reutt-Robey. Electrical detection of phase changes in adsorbed neutral dipolar molecules on graphene. *B. Am. Phys. Soc.*, 58, 2013.

[40] W.G. Schmidt, K. Seino, M. Preuss, A. Hermann, F. Ortmann, and F. Bechstedt. Organic molecule adsorption on solid surfaces: Chemical bonding, mutual polarisation and dispersion interaction. *Appl. Phys. A*, 85:387–397, 2006.

[41] S.K. Saha, R.C. Chandrakanth, H.R. Krishnamurthy, and U.V. Waghmare. Mechanisms of molecular doping of graphene: A first-principles study. *Phys. Rev. B*, 80:155414, 2009.

[42] D.J. Duchamp and R.E. Marsh. The Crystal Structure of Trimesic Acid (Benzene-1,3,5-tricarboxylic Acid). *Acta Cryst. B*, 25:5–19, 1969.

[43] S. Griessl, M. Lackinger, M. Edelwirth, M. Hietschold, and W.M. Heckl. Self-Assembled Two-Dimensional Molecular Host-Guest Architectures from Trimesic Acid. *Single Mol.*, 3:25–31, 2002.

[44] Y. Ye, W. Sun, Y. Wang, X. Shao, X. Xu, F. Cheng, J. Li, and K. Wu. A Unified Model: Self-Assembly of Trimesic Acid on Gold. *J. Phys. Chem. C*, 111:10138–10141, 2007.

[45] Y. Li, Z. Ma, K. Deng, S. Lei, Q. Zeng, X. Fan, S. De Feyter, W. Huang, and C. Wang. Thermodynamic Controlled Hierarchical Assembly of Ternary Supramolecular Networks at the Liquid-Solid Interface. *Chem. Eur. J.*, 15:5418–5423, 2009.

[46] M. Lackinger, S. Griessl, W.M. Heckl, M. Hietschold, and G.W. Flynn. Self-Assembly of Trimesic Acid at the Liquid-Solid Interface—a Study of Solvent-Induced Polymorphism. *Langmuir*, 21(11):4984–4988, 2005.

[47] M. Lackinger, S. Griessl, L. Kampshulte, F. Jamitzky, and W.M. Heckl. Dynamics of Grain Boundaries in Two-Dimensional Hydrogen-Bonded Molecular Networks. *Small*, 1:532–539, 2005.

[48] L. Kampshulte, M. Lackinger, A.-K. Maier, R.S.K. Kishore, S. Griessl, M. Schmittel, and W.M. Heckl. Solvent Induced Polymorphism in Supramolecular 1,3,5-Benzenetribenzoic Acid Monolayers. *J. Phys. Chem. B*, 110:10829–10836, 2006.

[49] M. Li, K. Deng, Y.-L. Yang, Q.-D. Zeng, M. He, and C. Wang. Electronically engineered interface molecular superlattices: STM study of aromatic molecules on graphite. *Phys. Rev. B*, 76:155438, 2007.

[50] S.J.H. Grießl. *Zweidimensionale Architekturen organischer Adsorbate: Untersuchung mittels STM, LEED, TDS, und Kraftfeldsimulationen*. PhD thesis, Technische Universität Chemnitz, 2003.

[51] A. Rochefort and J.D. Wuest. Interaction of Substituted Aromatic Compounds with Graphene. *Langmuir*, 25:210–215, 2009.

[52] S.J.H. Griessl, M. Lackinger, F. Jamitzky, T. Markert, M. Hietschold, and W.M. Heckl. Room-temperature scanning tunneling microscopy manipulation of single C_{60} molecules at the liquid-solid interface: Playing nanosoccer. *J. Phys. Chem. B*, 108(31):11556–11560, 2004.

[53] X. Dong, Y. Shi, Y. Zhao, D. Chen, J. Ye, Y. Yao, F. Gao, Z. Ni, T. Yu, Z. Shen, Y. Huang, P. Chen, and L.-J. Li. Symmetry breaking of graphene monolayers by molecular decoration. *Phys. Rev. Lett.*, 102(13):135501, 2009.

[54] B. Binnig and H. Rohrer. Scanning Tunneling Microscopy—from Birth to Adolescence (Nobel Lecture). In *Les Prix Nobel*, page 85, 1986.

[55] J. Tersoff and D.R. Hamann. Theory and application for the scanning tunneling microscope. *Phys. Rev. Lett.*, 50(25):1998–2001, 1983.

[56] J. Tersoff and D.R. Hamann. Theory of the scanning tunneling microscope. *Phys. Rev. B*, 31(2):805–813, 1985.

[57] Y. Kuk and P.J. Silverman. Scanning tunneling microscope instrumentation. *Rev. Sci. Instrum.*, 60(2):165–180, 1989.

[58] R.M. Feenstra, J.A. Stroscio, and A.P. Fein. Tunneling spectroscopy of the Si(111) 2×1 surface. *Surf. Sci.*, 181(1):295–306, 1987.

[59] R.J. Hamers. Atomic-resolution surface spectroscopy with the scanning tunneling microscope. *Annu. Rev. Phys. Chem.*, 40(1):531–559, 1989.

[60] Omicron Vakuumphysik GmbH. *The Variable Temperature STM User's Guide*, 1.3 edition, 1997.

[61] C. Bai. *Scanning Tunneling Microscopy and Its Applications*, pages 80–89. Springer, 2000.

[62] A.J. Melmed. The art and science and other aspects of making sharp tips. *J. Vac. Sci. Technol. B*, 9(2):601–608, 1991.

[63] G. Binnig, H. Rohrer, C. Gerber, and E. Weibel. 7×7 reconstruction on Si(111) resolved in real space. *Phys. Rev. Lett.*, 50(2):120–123, 1983.

[64] R.C. Henderson, R.B. Marcus, and W.J. Polito. Carbide contamination of silicon surfaces. *J. Appl. Phys.*, 42(3):1208–1215, 1971.

[65] D. Tománek, S.G. Louie, H.J. Mamin, D.W. Abraham, R.E. Thomson, E. Ganz, and J. Clarke. Theory and observation of highly asymmetric atomic structure in scanning-tunneling-microscopy images of graphite. *Phys. Rev. B*, 35:7790–7793, 1987.

[66] U. Neuwald, H.E. Hessel, A. Feltz, U. Memmert, and R.J. Behm. Initial stages of native oxide growth on hydrogen passivated Si(111) surfaces studied by scanning tunneling microscopy. *Appl. Phys. Lett.*, 60:1307, 1992.

[67] M. Lublow and H.J. Lewerenz. Real-time monitoring of SiO_2/Si(111) inter-layer etching by Brewster-angle reflectometry. *Surf. Sci.*, 602:1677–1687, 2008.

[68] M. Depas, T. Nigam, and M.M. Heyns. Soft breakdown of ultra-thin gate oxide layers. *IEEE T. Electron Dev.*, 43:1499–1504, 1996.

[69] B.R. Conrad, W.G. Cullen, B.C. Riddick, and E.D. Williams. Pentacene islands grown on ultra-thin SiO_2. *Surf. Sci. Lett.*, 603:L27–L30, 2009.

[70] J.G. Hou, J. Yang, H. Wang, Q. Li, C. Zeng, H. Lin, W. Bing, D.M. Chen, and Q. Zhu. Identifying Molecular Orientation of Individual C_{60} on a Si (111)-(7×7) Surface. *Phys. Rev. Lett.*, 83(15):3001–3004, 1999.

[71] J.A. Larsson, S.D. Elliott, J.C. Greer, J. Repp, G. Meyer, and R. Allenspach. Orientation of individual C_{60} molecules adsorbed on Cu(111): Low-temperature scanning tunneling microscopy and density functional calculations. *Phys. Rev. B*, 77(11):115434, 2008.

[72] W. Mickelson, S. Aloni, W.-Q. Han, J. Cumings, and A. Zettl. Packing C_{60} in boron nitride nanotubes. *Science*, 300(5618):467–469, 2003.

[73] R.C. Haddon, A.S. Perel, R.C. Morris, T.T.M. Palstra, A.F. Hebard, and R.M. Fleming. C_{60} thin film transistors. *Appl. Phys. Lett.*, 67(1):121–123, 1995.

[74] S. Kobayashi, T. Takenobu, S. Mori, A. Fujiwara, and Y. Iwasa. Fabrication and characterization of C_{60} thin-film transistors with high field-effect mobility. *Appl. Phys. Lett.*, 82:4581, 2003.

[75] W. Brütting, M. Bronner, M. Götzenbrugger, and A. Opitz. Ambipolar Blends of Cu-Phthalocyanine and Fullerene: Charge Carrier Mobility, Electronic Structure and their Implications for Solar Cell Applications. *Macromol. Symp.*, 268(1):38–42, 2008.

[76] G. Yu, J. Gao, J.C. Hummelen, F. Wudl, and A.J. Heeger. Polymer photovoltaic cells: Enhanced efficiencies via a network of internal donor-acceptor heterojunctions. *Science*, pages 1789–1790, 1995.

[77] J.J.M. Halls, K. Pichler, R.H. Friend, S.C. Moratti, and A.B. Holmes. Exciton diffusion and dissociation in a poly (p-phenylenevinylene)/C_{60} heterojunction photovoltaic cell. *Appl. Phys. Lett.*, 68(22):3120–3122, 1996.

[78] S. Yoo, B. Domercq, and B. Kippelen. Efficient thin-film organic solar cells based on pentacene/C_{60} heterojunctions. *Appl. Phys. Lett.*, 85(22):5427–5429, 2004.

[79] T. Arai, Y. Murakami, H. Suematsu, K. Kikuchi, Y. Achiba, and I. Ikemoto. Resistivity of single crystal C_{60} and effect of oxygen. *Solid State Commun.*, 84(8):827–829, 1992.

[80] E. Frankevich, Y. Maruyama, and H. Ogata. Mobility of charge carriers in vapor-phase grown C_{60} single crystal. *Chem. Phys. Lett.*, 214(1):39–44, 1993.

[81] M.A. Groce, B.R. Conrad, W.G. Cullen, A. Pimpinelli, E.D. Williams, and T.L. Einstein. Temperature-dependent nucleation and capture-zone scaling of C_{60} on silicon oxide. *Surf. Sci.*, 606:53–56, 2012.

[82] J.W. Evans, P.A. Thiel, and M.C. Bartelt. Morphological evolution during epitaxial thin film growth: Formation of 2D islands and 3D mounds. *Surf. Sci. Rep.*, 61(1):1–128, 2006.

[83] P.A. Mulheran and J.A. Blackman. Capture zones and scaling in homogeneous thin-film growth. *Phys. Rev. B*, 53(15):10261–10267, 1996.

[84] D. Weaire, J.P. Kermode, and J. Wejchert. On the distribution of cell areas in a Voronoi network. *Philos. Mag. B*, 53(5):L101–L105, 1986.

[85] J.-S. Ferenc and Z. Néda. On the size distribution of Poisson Voronoi cells. *Physica A*, 385(2):518–526, 2007.

[86] N.L. Johnson, S. Kotz, and N. Balakrishnan. *Continuous Univariate Distributions, vol. 1.* John Wiley & Sons, 1994.

[87] T. Kiang. Random fragmentation in two and three dimensions. *Z. Astrophys.*, 64:433, 1966.

[88] A. Pimpinelli and T.L. Einstein. Capture-zone scaling in island nucleation: Universal fluctuation behavior. *Phys. Rev. Lett.*, 99:226102, 2007.

[89] T.L. Einstein and O. Pierre-Louis. Implications of random-matrix theory for terrace-width distributions on vicinal surfaces: Improved approximations and exact results. *Surf. Sci.*, 424(1):L299–L308, 1999.

[90] A.Y. Abul-Magd. Superstatistics in random matrix theory. *Physica A*, 361(1):41–54, 2006.

[91] A. Pimpinelli and T.L. Einstein. Pimpinelli and Einstein Reply. *Phys. Rev. Lett.*, 104:149602, 2010.

[92] M. Li, Y. Han, and J.W. Evans. Comment on "Capture-Zone Scaling in Island Nucleation: Universal Fluctuation Behavior". *Phys. Rev. Lett.*, 104:149601, 2010.

[93] F. Shi, Y. Shim, and J.G. Amar. Capture-zone areas in submonolayer nucleation: Effects of dimensionality and short-range interactions. *Phys. Rev. E*, 79(1):011602, 2009.

[94] D.L. González, A. Pimpinelli, and T.L. Einstein. Spacing distribution functions for the one-dimensional point-island model with irreversible attachment. *Phys. Rev. E*, 84(1):011601, 2011.

[95] R. Sathiyanarayanan, A.B.H. Hamouda, A. Pimpinelli, and T.L. Einstein. Role of codeposited impurities during growth. II. Dependence of morphology on binding and barrier energies. *Phys. Rev. B*, 83(3):035424, 2011.

[96] J.G. Amar and F. Family. Critical cluster size: Island morphology and size distribution in submonolayer epitaxial growth. *Phys. Rev. Lett.*, 74(11):2066–2069, 1995.

[97] T.-L. Chan, C.Z. Wang, M. Hupalo, M.C. Tringides, and K.M. Ho. Quantum Size Effect on the Diffusion Barriers and Growth Morphology of Pb/Si(111). *Phys. Rev. Lett.*, 96:226102, 2006.

[98] S.M. Binz, M. Hupalo, and M.C. Tringides. Height-dependent nucleation and ideal layer by layer growth in Pb/Pb(111)/Si(111). *Phys. Rev. B*, 78:193407, 2008.

[99] S.M. Binz, M. Hupalo, and M.C. Tringides. Quantum size effect dependent critical size cluster and finite size effects. *J. Appl. Phys.*, 105:094307, 2009.

[100] A. Pimpinelli and R. Ferrando. Reentrant morphological instability of epitaxial islands. *Phys. Rev. B*, 60(24):17016, 1999.

[101] M. Fanfoni, E. Placidi, F. Arciprete, E. Orsini, F. Patella, and A. Balzarotti. Sudden nucleation versus scale invariance of InAs quantum dots on GaAs. *Phys. Rev. B*, 75(24):245312, 2007.

[102] M. Fanfoni, F. Arciprete, C. Tirabassi, D. Del Gaudio, A. Filabozzi, A. Balzarotti, F. Patella, and E. Placidi. Coarsening effect on island-size scaling: The model case InAs/GaAs(001). *Phys. Rev. E*, 86(6):061605, 2012.

[103] M. Fanfoni, E. Placidi, F. Arciprete, E. Orsini, F. Patella, and A. Balzarotti. Experimental corroboration of the Mulheran-Blackman explanation of the scale invariance in thin film growth: The case of InAs quantum dots on GaAs(001). *arXiv preprint cond-mat/0610118*, 2006.

[104] F. Arciprete, E. Placidi, V. Sessi, M. Fanfoni, F. Patella, and A. Balzarotti. How kinetics drives the two- to three-dimensional transition in semiconductor strained heterostructures: The case of InAs/GaAs(001). *Appl. Phys. Lett.*, 89(4):041904, 2006.

[105] S. Lorbek, G. Hlawacek, and C. Teichert. Determination of critical island size in para-sexiphenyl islands on SiO$_2$ using capture-zone scaling. *Eur. Phys. J. - Appl. Phys.*, 55(02), 2011.

[106] M. Kotrla, J. Krug, and P. Šmilauer. Submonolayer epitaxy with impurities: Kinetic Monte Carlo simulations and rate-equation analysis. *Phys. Rev. B*, 62(4):2889, 2000.

[107] S.J.H. Griessl, M. Lackinger, F. Jamitzky, T. Markert, M. Hietschold, and W.M. Heckl. Incorporation and manipulation of coronene in an organic template structure. *Langmuir*, 20(21):9403–9407, 2004.

[108] R. Liu, K.-F. Mok, and S. Valiyaveettil. Solid-state self-assembly of a complex from 1,3,5-benzenetricarboxylic acid and 1,3,5-trihydroxybenzene: Influence of strong O–H···O and C–H···O hydrogen bonds. *New J. Chem.*, 25(7):890–892, 2001.

[109] Two-dimensional molecular porous networks constructed by surface assembling. *Coordin. Chem. Rev.*, 253(2324):2959–2979, 2009.

[110] X. Zhang, S.-S. Li, T. Chen, D. Wang, and L.-J. Wan. Molecular templates for controlling and ordering organic molecules on solid surfaces. *Nano*, 07(01):1230001, 2012.

[111] J. Morales-Cifuentes and T.L. Einstein. A theoretical study of symmetry-breaking organic overlayers on single- and bi-layer graphene. *B. Am. Phys. Soc.*, 58, 2013.

[112] G. Li, A. Luican, and E.Y. Andrei. Scanning tunneling spectroscopy of graphene on graphite. *Phys. Rev. Lett.*, 102(17):176804, 2009.

[113] B.R. Conrad. *Interface Effects on Nanoelectronics*. PhD thesis, University of Maryland, 2009.